

# 1 Sensitivity of the Eocene Climate to CO<sub>2</sub> and Orbital Variability

2 John S. Keery<sup>1</sup>, Philip B. Holden<sup>1</sup>, Neil R. Edwards<sup>1</sup>

3 <sup>1</sup>School of Environment, Earth & Ecosystem Sciences, The Open University, Milton Keynes, MK7 6AA, UK

4 *Correspondence to:* John S. Keery (john.keery@open.ac.uk)

5 **Abstract.** The early Eocene, from about 56 Ma, with high atmospheric CO<sub>2</sub> levels, offers an analogue for the response of the  
6 Earth's climate system to anthropogenic fossil fuel burning. In this study we present an ensemble of 50 Earth system model  
7 runs with an early Eocene palaeogeography and variation in the forcing values of atmospheric CO<sub>2</sub> and the Earth's orbital  
8 parameters. Relationships between simple summary metrics of model outputs and the forcing parameters are identified by  
9 linear modelling, providing estimates of the relative magnitudes of the effects of atmospheric CO<sub>2</sub> and each of the orbital  
10 parameters on important climatic features, including tropical-polar temperature difference, ocean-land temperature contrast,  
11 Asian, African and S. American monsoon rains, and climate sensitivity. Our results indicate that although CO<sub>2</sub> exerts a  
12 dominant control on most of the climatic features examined in this study, the orbital parameters also strongly influence  
13 important components of the ocean-atmosphere system in a greenhouse Earth. In our ensemble, atmospheric CO<sub>2</sub> spans the  
14 range 280 - 3000 ppm, and this variation accounts for over 90% of the effects on mean air temperature, southern winter high-  
15 latitude ocean-land temperature contrast and northern winter tropical-polar temperature difference. However, the variation  
16 of precession accounts for over 80% of the influence of the forcing parameters on the Asian and African monsoon rainfall,  
17 and obliquity variation accounts for over 65% of the effects on winter ocean-land temperature contrast in high northern  
18 latitudes, and northern summer tropical-polar temperature difference. Our results indicate a bimodal climate sensitivity, with  
19 values of 4.36°C and 2.54°C, dependent on low or high states of atmospheric CO<sub>2</sub> concentration respectively, with a  
20 threshold at approximately 1000 ppm in this model, and due to a saturated vegetation-albedo feedback. Our method gives a  
21 quantitative ranking of the influence of each of the forcing parameters on key climatic model outputs, with additional spatial  
22 information from singular value decomposition providing insights into likely physical mechanisms. The results demonstrate  
23 the importance of orbital variation as an agent of change in climates of the past, and we demonstrate that emulators derived  
24 from our modelling output can be used as rapid and efficient surrogates of the full complexity model, to provide estimates of  
25 climate conditions from any set of forcing parameters.

## 26 1 Introduction

27 In the early Eocene several episodes of global warming coincided with carbon isotope excursions (CIEs), pulses of  
28 isotopically light carbon injected into the atmosphere and oceans, and recorded in high-resolution marine and terrestrial  
29 sediments (Kennett and Stott, 1991). In one large CIE, at the Palaeocene-Eocene transition at ~56 Ma, the Palaeocene-

1 Eocene Thermal Maximum (PETM), evidence from both tropical (e.g. Zachos et al., 2003) and polar (e.g. Sluijs et al., 2006)  
2 regions indicates that temperatures increased by  $\sim 5^{\circ}\text{C}$  in less than 10 kyr. Although the greenhouse gas (GHG) sources, and  
3 the duration of the onset phase of the PETM are uncertain, the relatively short time scale and global extent of the PETM  
4 strongly suggest that a large and sudden increase in GHGs in the atmosphere was the primary climatic forcing factor (Zachos  
5 et al., 2007). Since the PETM is the most recent period in Earth's history for which estimated atmospheric GHG  
6 concentrations are similar in magnitude to those of the present-day, and expected to arise from fossil fuel burning, the PETM  
7 may provide a valuable analogue for anthropogenic climate change (e.g. McInerney and Wing, 2011; Zeebe et al., 2016;  
8 Zeebe and Zachos, 2013).

9 The CIEs of the early Eocene show similar regularity in their timing to periodic changes in the Earth's orbit around the sun  
10 (Lourens et al., 2005), and the search for causal relationships between orbital cycles and Paleogene climate is an active area  
11 of research (e.g. Lauretano et al., 2015; Laurin et al., 2016; Lunt et al., 2011).

12 Although the climatic state in the early Eocene cannot be directly measured, much information on temperature and  
13 biogeochemical conditions can be inferred from measurements of proxy data: preserved natural records of climate  
14 variability, which can be linked to the property of interest through physical processes (Jones and Mann, 2004). But there are  
15 major uncertainties in proxy data from the Eocene due to incomplete preservation and alteration over time, with additional  
16 uncertainties as to the seasonality of contributory processes, and for ocean proxies, the depth at which the property of  
17 interest, e.g. temperature, influences the proxy (Dunkley Jones et al., 2013). Climate models therefore have an important  
18 role to play in exploring the mechanistic functioning of palaeoclimates (Huber, 2012).

19 Climate simulations with high temporal and spatial resolution can be obtained from General Circulation Models (GCMs),  
20 but the requirement of GCMs for powerful computers and long run-times makes them difficult to deploy for large ensembles  
21 of model simulations and restricts their ability to investigate the large uncertainties in forcings and model parameterisations.  
22 Such ensembles are more practical with more heavily parameterised and hence more computationally efficient Earth system  
23 Models of Intermediate Complexity (EMICs), (Weber, 2010), although we note that Araya-Melo et al. (2015) and Lord et al.  
24 (2017) have deployed the GCM HadCM3 in ensemble-based studies of orbital forcing effects on climates of the Pleistocene  
25 and late Pliocene respectively.

26 In this study we deploy an EMIC, PLASIM-GENIE (Holden et al., 2016), in an ensemble of model runs to investigate the  
27 effects of varying GHG concentration and orbital parameters on the palaeoclimate of the Earth, with an Eocene configuration  
28 of the oceans and continents. We reduce the dimensionality of the model output by computing simple scalar metrics to  
29 denote key climatic features of each ensemble member, and we apply singular value decomposition (SVD) to identify the  
30 principal components (PCs) of temperature and precipitation fields in the full ensemble, for comparison with the variation in  
31 the forcing parameters.

32 By applying the linear modelling and emulation methods of Holden et al. (2015), we regress both the simple scalar metrics  
33 and the SVD reduced dimension model outputs onto the forcing parameters, and from the derived relationships, we infer  
34 main effects denoting the effect of each explanatory term in the linear model, and total effects denoting the effect of each

1 forcing parameter, on the variation in the scalar metrics and on the temperature and precipitation output fields. We  
2 demonstrate that emulators derived in respect of tropical precipitation metrics can be used to estimate Eocene monsoonal  
3 responses to any combination of GHG and orbital forcing parameter values.

## 4 **2 The Early Eocene and the PETM**

### 5 **2.1 Climate of the Early Eocene**

6 During the Eocene, the Earth remained in the ‘greenhouse’ state, which had persisted since the early Cretaceous, with polar  
7 air temperatures remaining above 0°C for most of the year (Wing and Greenwood, 1993), no permanent polar ice-caps,  
8 reduced equator-pole temperature gradients, and lower ocean-land temperature contrasts, inferred from fossil and isotope  
9 indicators of temperature and environmental conditions. Climate modellers have experienced difficulty in simulating  
10 Cretaceous and Palaeogene ‘equable climates’ (Sloan and Barron, 1990; Wing and Greenwood, 1993) with sufficient  
11 warming at high latitudes, without overheating the tropics, although Huber and Caballero (2011), hereafter HC11, have  
12 demonstrated that with sufficiently high levels of CO<sub>2</sub> (as a proxy for all forms of radiative forcing), climate models can  
13 generate global air temperature distributions in broad agreement with the proxy temperature measurements.

14 The onset of the PETM, at approximately 55.9 Ma (Westerhold et al., 2009), is recognised as the boundary between the  
15 Palaeocene and Eocene epochs (Aubry et al., 2007), and is characterised by a large CIE, indicating large GHG emissions,  
16 accompanied by a sudden rise in global temperature (Kennett and Stott, 1991), extensive extinction and origination of  
17 nannoplankton (Gibbs et al., 2006), and widespread ocean anoxia (Dickson et al., 2012). There is some evidence from  
18 analysis and modelling of the timing and duration of variations in  $\delta^{13}\text{C}$  and  $\delta^{18}\text{O}$  observed in nannoplankton fossils that some  
19 of the GHG emissions were initially in the form of CH<sub>4</sub> (Dickens, 2011; Lunt et al., 2011; Thomas et al., 2002), which is  
20 rapidly oxidised in the atmosphere to CO<sub>2</sub>. The PETM is also marked by enhanced precipitation and continental weathering  
21 (Carmichael et al., 2016; Chen et al., 2016; Penman, 2016), rapid and sustained surface ocean acidification (Penman et al.,  
22 2014; Zachos et al., 2005), and shares many features of the global-scale oceanic anoxic events of the Cretaceous and Jurassic  
23 periods (Jenkyns, 2010). See McInerney and Wing (2011) for a review of PETM research.

24 The duration of the onset phase of the PETM is uncertain. Cui et al. (2011) have suggested that the peak rate of addition of  
25 CO<sub>2</sub> to the atmosphere was much lower than the present-day rate of anthropogenic GHG emissions, but this is disputed by  
26 Sluijs et al. (2012). Zeebe et al. (2016) have estimated that the initial release of carbon at the onset of the PETM lasted at  
27 least 4 kyr, at a rate which was little more than one tenth of the present rate of anthropogenic emissions, so the Earth may  
28 already be in a ‘no-analogue’ state, with anthropogenic climate change likely to exceed that of the PETM. However rapid the  
29 onset, the greenhouse conditions of the early Eocene, and particularly the PETM, provide an opportunity to apply lessons  
30 from the past, with a view to improving predictions of the future (Lunt et al., 2013).

## 1 **2.2 Palaeogeography of the Early Eocene**

2 The arrangement of the continents and oceans in the Early Eocene was broadly similar to that of the present, with the Earth's  
3 land mass divided into the same major continents, and with most of the land mass in the northern hemisphere. India had not  
4 yet collided with the Eurasian continent, and the closure of the Tethys Ocean was not yet complete. Such tectonic  
5 movements may have effected some changes to the climate system. In particular, the configuration of ocean gateways  
6 strongly influences modes of ocean circulation, and hence affects energy transport throughout the climate system (Lunt et al.,  
7 2016; Sijp et al., 2014).

### 8 **2.2.1 Continental and Ocean Configurations during the Early Eocene**

9 Although the Bering Strait was closed throughout the Palaeogene (Marincovich et al., 1990), and the Western Interior  
10 Seaway linking the Arctic to the Pacific was closed by the end of the Cretaceous (Slattery et al., 2015), the Arctic Ocean was  
11 connected to the major oceans during the early Eocene through the Turgai Strait, also known as the Western Siberian  
12 Seaway (Akhmetiev et al., 2012; Radionova and Khokhlova, 2000). The Lomonosov Ridge, from which core samples have  
13 been obtained by the Arctic Coring Expedition (ACEX) of the Integrated Ocean Drilling Program Expedition (IODP) 302  
14 (Backman et al., 2008), was on the edge of the Arctic basin rather than across the pole as in the present configuration  
15 (O'Regan et al., 2008).

16 Both the Drake Passage between South America and Antarctica (Barker and Burrell, 1977) and the Tasman Gateway  
17 between Australia and Antarctica (Exon et al., 2004) were closed during the early Eocene, preventing the development of an  
18 Antarctic Circumpolar Current and allowing greater southern hemisphere meridional heat transport than in the modern  
19 world.

### 20 **2.2.2 Orbital Configurations**

21 Throughout Earth's geological history, oscillations in the relative positions of the Earth and Sun have influenced both the  
22 Earth's climate, and rates of sedimentation in some climate-sensitive environmental settings (Hinnov and Hilgen, 2012). The  
23 main oscillations are the eccentricity of the Earth's orbit around the Sun, with periods of ~100 kyr and 405 kyr, the obliquity  
24 or tilt of the Earth's axis of rotation, with a period of ~40 kyr, and precession, the relative timing between perihelion and the  
25 seasons, with a period of ~20 kyr (Berger et al., 1993). By correlating oscillations preserved in the geological record with  
26 computed time series of changes in insolation received by the Earth, an absolute astronomical time scale may be constructed  
27 for recent time-spans with a complete sedimentary record, but where the geological evidence is incomplete, or where  
28 uncertainties in the orbital model are too great further back in time, only a relative time scale may be derived (Hilgen et al.,  
29 2010). An absolute astronomical solution has been computed back to 50 Ma (Laskar et al., 2011), and an absolute age of  
30  $55.53 \pm 0.05$  Ma has been proposed for the onset of the PETM at the start of the Eocene epoch by Westerhold et al. (2012).

1 Lourens et al. (2005) noted the apparent astronomical pacing of global warming events in the late Palaeocene and early  
2 Eocene, with correlations to both the long and short periods of eccentricity. Sexton et al. (2011) suggested that although the  
3 smaller hyperthermal events of the early Eocene were driven by cycles of carbon sequestration and release in the ocean,  
4 paced by the eccentricity cycles, the PETM was likely to have been driven by carbon injection from a sedimentary source.  
5 Laurin et al. (2016) applied a method which allows the phase of the 405 kyr eccentricity cycle to be identified from  
6 interference patterns and frequency modulation of the ~100 kyr eccentricity cycle, and concluded that four hyperthermals in  
7 the early Eocene were initiated at 405 kyr eccentricity maxima, but in a study of terrestrial sediments with apparent  
8 correlation to the ~100 kyr eccentricity cycle, Smith et al. (2014) suggested that hyperthermals occurred during eccentricity  
9 minima, rather than maxima.

## 10 **3 Methods**

### 11 **3.1 The PLASIM-GENIE Model**

12 PLASIM-GENIE (Holden et al., 2016) is an intermediate complexity AOGCM. We apply the model at a spectral T21  
13 atmospheric resolution, which corresponds to a triangular truncation applied at wave number 21 and a horizontal resolution  
14 of 5.625°, with 10 layers, and a matching ocean grid with 32 depth levels. We apply the calibrated parameter set of Holden  
15 et al (2016). The component modules are as follows:

16 PLASIM (Fraedrich, 2012) is built around the 3D primitive equation atmosphere model PUMA (Fraedrich et al., 2005). The  
17 radiation scheme considers two wavelength bands in the short wave and uses the broad band emissivity method for long  
18 wave. Fractional cloud cover is diagnosed. Other parameterised processes include large-scale precipitation, cumulus and  
19 shallow convection, dry convection and boundary layer heat fluxes.

20 GOLDSTEIN is a 3D frictional-geostrophic ocean model (Edwards and Marsh, 2005; Marsh et al., 2011), dynamically  
21 similar to classical GCMs, except that it neglects momentum advection and acceleration. Barotropic flow around the four  
22 continental islands (Fig. 1) is derived from linear constraints that arise from integrating the depth-averaged momentum  
23 equations.

24 GOLDSTEINSEAICE (Edwards and Marsh, 2005) solves for the fraction of the ocean surface covered by ice within a grid  
25 cell and for the average sea-ice height. A diagnostic equation is solved for the ice surface temperature. Growth or decay of  
26 sea ice depends on the net heat flux into the ice (Hibler III, 1979; Semtner Jr, 1976). Sea-ice dynamics are represented by  
27 diffusion and advection by surface currents.

28 ENTS (Williamson et al., 2006) models vegetative and soil carbon densities, assuming a single plant functional type.  
29 Photosynthesis depends upon temperature (with a double-peaked response representing boreal and tropical forest),  
30 atmospheric CO<sub>2</sub> concentration and soil moisture availability. Self-shading is parameterised. Land surface albedo, moisture  
31 bucket capacity and surface roughness are parameterised in terms of the simulated carbon pool densities.

1 The computational efficiency of PLASIM-GENIE is achieved mainly through low spatial resolution ( $\sim 5^\circ$ ) and, relative to  
2 high-complexity Earth system models, simplifying assumptions in physical processes. These include, for instance,  
3 simplified parameterisations of radiative transport and convection in the atmosphere, the neglect of momentum transport in  
4 the ocean, and the representation of all vegetation as a single plant functional type. Climate sensitivity, the response of the  
5 climate to a doubling of atmospheric  $\text{CO}_2$  concentration, including feedbacks, is an emergent property of the model.

## 6 **3.2 Model Configuration**

### 7 **3.2.1 Model Grid**

8 This study was designed before Lunt et al. (2017) presented their 'DeepMIP' guidelines for model simulations of the latest  
9 Paleocene and early Eocene. However, our palaeogeography is based on the high-resolution digital reconstruction of the  
10 early Eocene published by Herold et al. (2014), and which Lunt et al. (2017) recommended should be used as the standard  
11 for all palaeoclimate simulations within the DeepMIP framework. We have used the dataset of Herold et al. (2014) as an  
12 initial configuration for the tectonic layout, topography and bathymetric boundary conditions in our study. We have reduced  
13 the resolution of the Eocene palaeogeography provided by Herold et al. (2014) to a configuration of 64 longitude x 32 latitude  
14 cells, with each cell representing  $5.625^\circ$  in each orientation. Cells at high latitudes therefore represent smaller land areas than  
15 cells at low latitudes. Our vertical resolution is 32 ocean depths and 10 atmospheric layers. We have incorporated the ocean  
16 gateway configurations discussed in section 2.1.1. The Turgai Strait is open in our configuration, and is the only connection  
17 between the Arctic Ocean and other oceans. The Drake Passage and Tasman Gateway are both closed.

18 The palaeogeography (Fig. 1) comprises four land masses: N America and Eurasia; Antarctica combined with S America and  
19 Australia; Africa; and India. Red rectangles in Fig. 1 indicate the boundaries of areas used to calculate simple metrics of  
20 centennially averaged seasonal precipitation, as empirical indicators of African, Asian and S. American monsoons.

### 21 **3.2.2 Forcing and Other Input Parameters**

22 In order to investigate the sensitivity of the Eocene climate to variation in atmospheric  $\text{CO}_2$  and orbital parameters, we have  
23 constructed an ensemble of 50 model configurations, each with a unique set of forcing parameters comprising atmospheric  
24  $\text{CO}_2$ , eccentricity ( $e$ ), obliquity ( $\varepsilon$ ) and precession ( $\omega$ ), the angle on the Earth's orbit around the Sun between the moving  
25 vernal equinox and the longitude of perihelion (Berger et al., 1993). When  $e$  is zero, the Earth's distance from the Sun is  
26 constant at all points on the orbit, so there is no precessional effect. The magnitude of precessional effects is controlled by  $e$ ,  
27 while phase is controlled by  $\omega$ , so precessional effects are commonly described by the precession index given by  $e \sin \omega$ . The  
28 precession index is at its maximum value when perihelion occurs at the December solstice, its minimum value when  
29 perihelion is at the June solstice, and has a value of 0.0 when perihelion is at either the March or September equinox. The  
30 only orbital parameter which alters the total annual solar radiation received by the Earth is  $e$ , although the range of variation  
31 is very small. We include  $e$  and  $\omega$  as separate and independent forcing parameters, rather than combined as the precession

1 index, or in the form  $e\cos\omega$ . An additional dummy parameter is included to test for possible overfitting of relationships  
2 between forcing parameters and model output fields.

3 Although the maximum mass of CO<sub>2</sub> injected into the atmosphere during CIEs, and in particular the PETM, remains  
4 uncertain, there is broad agreement that the atmospheric concentration of CO<sub>2</sub> did not exceed 3000 ppm (e.g. Gehler et al.,  
5 2016), and that it did not fall below the pre-industrial level of 280 ppm at any time during the early Eocene. We allocate  
6 these values as the limits of a uniform range from which our ensemble of CO<sub>2</sub> values is selected.

7 Since the absolute astronomical time scale for the early Eocene has an uncertainty which is greater than the periods of the  
8 obliquity and precession cycles, and there remains disagreement as to which phases of the eccentricity cycles are related to  
9 CIEs, there are no combinations of the orbital forcing parameters which can be known a priori to be of greater importance in  
10 their effects on the Eocene climate in general, and on their contributions to the initiation, duration and termination of the  
11 CIEs in particular. We therefore select values of orbital parameters independently, and from the full range of each  
12 parameter's variation during the early Eocene.

13 To ensure the best coverage of the five-dimensional state-space comprised of the four forcing parameters and the additional  
14 dummy parameter in a limited number of model runs, we apply the Latin hypercube method (McKay et al., 1979), a  
15 constrained Monte Carlo sampling scheme in which the range to be sampled for each variable is divided into non-  
16 overlapping intervals, and one value from each interval is randomly selected (Wyss and Jorgensen, 1998). This provides  
17 adequate coverage of the state space more efficiently than can be achieved by a simple Monte-Carlo sampling approach  
18 (Rougier, 2007). The present study has been designed to facilitate direct comparison between the results for specific  
19 ensemble members and their direct counterparts in a future study using the EMIC model GENIE-1 (Edwards and Marsh,  
20 2005), which will include additional forcing parameters not used by this PLASIM-GENIE study. We have applied an  
21 iterative method to generate a pair of corresponding hypercubes with five and eleven dimensions for the PLASIM-GENIE  
22 and GENIE-1 studies respectively, in which the minimum Euclidean distance between any two points is maximised, and  
23 linear correlation between any two parameters is minimised. We note that our selection of values for  $\omega$ , an angular  
24 parameter, is from 0-360°, treated as a linear range, with the consequence that the maximin criterion within the Latin  
25 hypercube algorithm is incorrectly calculated. However, given the dimensionality of our experimental design, this is  
26 unlikely to result in a significant reduction in the efficiency with which design points are distributed throughout the very  
27 sparsely populated state-space. We draw readers' attention to an approach presented by Bounceur et al. (2015), in which  
28 independent values of  $e\sin\omega$ ,  $e\cos\omega$  and  $\varepsilon$  are sampled, with rejection of absolute values of  $e\sin\omega$  and  $e\cos\omega$  which equal or  
29 exceed the maximum value of  $e$ . This experimental design allows values of  $e$  and  $\omega$  for any design point to be identified by  
30 trigonometric analysis, while efficiently sampling the state space. Details of the steps taken to generate the hypercubes are  
31 provided in Appendix A. The absolute value of the r correlation coefficient does not exceed 0.1 for any pair of input  
32 (forcing and dummy) parameters. Uniform ranges for each of the forcing parameters and the dummy parameter are shown in  
33 Table 1, and the values applied in all 50 PLASIM-GENIE ensemble members are shown in Table 2.

1 The intensity of radiation emitted by the Sun has increased steadily over time, and we apply the linear model of Gough  
2 (1981), and select a solar constant of  $1358.68 \text{ W m}^{-2}$ . We note that Lunt et al. (2017) have recommended that a modern  
3 value of  $1361.0 \text{ W m}^{-2}$  should be applied to studies within the DeepMIP framework, in order to facilitate comparison  
4 between simulations with modern and pre-industrial levels of  $\text{CO}_2$ , and to offset the absence of elevated levels of  $\text{CH}_4$ .

### 5 **3.2.3 Running the Models**

6 Each simulation was run for a spin-up period of 1000 years to reach a quasi-steady state, with key output fields recorded as  
7 seasonal averages for each of the three-month periods December, January and February (DJF) and June, July and August  
8 (JJA), representing both winter and summer seasons in both the northern and southern hemispheres. Although model output  
9 includes time series of some fields and output values every 100 years, in this study only the field values recorded at the end  
10 of the 1000 years of modelling are used for analysis of the results.

## 11 **3.3 Analysis of Model Output**

12 Comparison of the forcing parameters applied in the ensemble with the model output fields can be more efficiently achieved  
13 by reducing the dimensionality of the model output while retaining information on key components of the climate system.

### 14 **3.3.1 Simple Metrics**

15 In studies of the Earth's modern climate, it is recognised that the tropical-polar temperature difference (TPTD) influences  
16 poleward energy flux, and the ocean-land temperature contrast (OLC) affects monsoon intensity (Jain et al., 1999; Karoly  
17 and Braganza, 2001; Peixoto and Oort, 1992). Although atmospheric circulation patterns in the early Eocene will have  
18 differed from those in the modern world, in selecting latitude regions to represent the TPTD, we adopt the approach of Abbot  
19 and Tziperman (2008), who configured their model of the Cretaceous climate with latitude ranges of  $0\text{--}30^\circ$ ,  $30\text{--}60^\circ$ , and  $60\text{--}$   
20  $90^\circ$ , the approximate boundaries of the Hadley, Ferrel and Polar cells observed in the modern world (Peixoto and Oort,  
21 1992). On our model grid in which each cell spans  $5.625^\circ$  of latitude, for the purposes of deriving scalar metrics, we define  
22 the tropical regions to be between  $0.0^\circ$  and  $33.75^\circ$  North and South, and the polar regions to be between  $56.25^\circ$  to  $90^\circ$  North  
23 and South.

24 From the output values of air temperature in the lowest level of the atmosphere, weighted by grid cell area, we derive scalar  
25 values for each model run, of global annual mean air temperature (MAT), northern and southern hemisphere seasonality  
26 (mean area-weighted DJF-JJA temperature differences in the above-defined polar regions), TPTD for summer and winter in  
27 each hemisphere, and OLC for summer and winter in tropical and polar regions in each hemisphere.

28 Monsoons are related to seasonal variations in tropical and subtropical winds and precipitation (Trenberth et al., 2006).  
29 Wang and Fan (1999) noted that the choice of an index to denote monsoon behaviour in the modern world is difficult and  
30 arbitrary, with commonly applied indices based on average summer precipitation, maximum summer precipitation, winter-  
31 summer difference in precipitation, or wind circulation patterns within defined geographical areas. In this study, we derive

1 simple scalar metrics to denote indices for monsoons for Asia, Africa and South America by subtracting winter rainfall from  
2 summer rainfall, for defined geographical regions, denoted on Fig. 1, and selected for their similarity to monsoonal regions  
3 in the modern continental configuration.

### 4 **3.3.2 Singular Value Decomposition, Linear Modelling and Model Emulation**

5 We perform a singular value decomposition to identify the PCs and empirical orthogonal functions (EOFs) of temperature  
6 and precipitation fields in the full ensemble, although we note that climate variability may not be due to physical processes  
7 which vary orthogonally, and identification of PCs can be influenced by aspects of the experimental design. A detailed  
8 presentation of the use of this method in the analysis of climate data is given by Hannachi (2004).

9 We use the linear modelling method of Holden et al. (2015), to regress both the simple scalar metrics and the SVD reduced  
10 dimension model outputs onto the forcing parameters. Values of the forcing parameters  $\text{CO}_2$ ,  $e$  and  $\varepsilon$  (with its very small  
11 angular range considered to be approximately linear) were normalised to the range  $[-1, 1]$  and combined with  $\sin\omega$  and  $\cos\omega$   
12 to form 50-element column vectors representing the forcing factors. Each 2-D ( $32 \times 64$ ) result field for each ensemble  
13 member was unrolled to form a column vector of 2048 elements, comprising a single column within a  $2048 \times 50$  matrix of  
14 full ensemble values.

15 SVD was applied to decompose the full ensemble matrix for each 2-D result field, providing a  $2048 \times 50$  matrix of PCs, a  $50$   
16  $\times 50$  matrix of PC scores, and a  $50 \times 50$  matrix of diagonal values.

17 Linear modelling was applied to determine relationships between the normalised forcing factors and the first six columns of  
18 the PC scores, including products of pairs of forcing factors, and squares of each forcing factor, with the best fitting  
19 relationships selected according to the Akaike information criterion (Akaike, 1974) then refined using Bayes information  
20 criterion (Schwarz, 1978). Burnham and Anderson (2003) provide a detailed discussion of the application of information  
21 criteria in model selection. The resulting relationship provides a simple emulator which can be used to estimate a PC score  
22 for the 2-D model field, given a single set of forcing parameter values. Applying derived emulators in respect of temperature  
23 and precipitation for both seasons, demonstrated high correlation between emulated PC scores and PC scores derived  
24 directly through SVD (Table 3).

25 Our emulator approach uses linear regression, rather than a Gaussian process (GP), and is therefore simpler than the methods  
26 applied by Bounceur et al. (2015) in a study of the response of the climate-vegetation system in interglacial conditions to  
27 astronomical forcing, and by Araya-Melo et al. (2015) in their study of the Indian monsoon in the Pleistocene. Unlike linear  
28 models, GP models are intrinsically stochastic and give a more accurate quantification of their own error in emulating the  
29 input data. However, GP models can become computationally demanding in high dimensional space, and their results can be  
30 more difficult to interpret.

31 In order to analyse the results of each of our linear models, we apply the method described in detail by Holden et al. (2015)  
32 to derive the main effects (Oakley and O'Hagan, 2004), which provide a measure of the variation in the linear model output  
33 due to each of the terms (first order, second order and cross products), derived from their coefficients, and total effects

1 (Homma and Saltelli, 1996), which separate the effect of each forcing parameter on the variation in the model output.  
2 Although the forcing factors are all scaled within the range [-1, 1], the trigonometrical precession terms are not uniformly  
3 distributed across this range. We have therefore computed the variances of the first order, second order and cross product  
4 terms directly for all parameters, rather than applying the respective approximations of  $\frac{1}{3}$ ,  $\frac{1}{9}$  and  $\frac{4}{45}$ , and we have  
5 applied these values as scaling factors in calculating the main effects and total effects.

## 6 **4 Results**

### 7 **4.1 Model Output - Temperature and Precipitation**

8 Analysis of the model results has focused on variation in surface air temperature and precipitation in both winter and  
9 summer in each hemisphere, although it should be noted that our experiment has not been designed such that mean values in  
10 our ensemble output represent direct estimates of the Eocene climate mean. In the left column of Fig. 2, median  
11 temperatures at each grid cell for the full ensemble are plotted for DJF (top) and for JJA (bottom), with the standard  
12 deviations plotted in the right column.

13 Ranges of median temperatures over land are greater than over the oceans, but TPTD is smaller in both seasons and both  
14 hemispheres than simulated in the modern world (see Fig. 2, Holden et al 2016). It is apparent from the standard deviation  
15 field that the tropical-polar temperature difference varies substantially across the ensemble, particularly in northern winter.  
16 The temperature distributions are similar to those of the 2240 ppm CO<sub>2</sub> simulation of HC11, regarded as their “mid to late  
17 Eocene” analogue (they consider elevated CO<sub>2</sub> as a proxy for all radiative forcing, including uncertain climate sensitivity).  
18 The principal difference is in high northern latitude winter temperatures; the Arctic ocean remains above freezing in HC11.  
19 We note that the Arctic winter median air temperature is below freezing over both land and sea in the PLASIM-GENIE  
20 ensemble, (see Fig 3) and the Arctic does not remain ice-free throughout the year in any of the 50 simulations in our study.  
21 Tropical temperatures in excess of 35°C were simulated in some cases, as in HC11, which they regarded as their “most  
22 troubling result”, although they note observational data is currently insufficient to rule this out. Finally, we note that multi-  
23 model ensembles have found significant inter-model differences including, for instance a 9°C spread in global average  
24 temperature under the same CO<sub>2</sub> forcing (Lunt et al 2012). Quantification of model-related uncertainty is beyond the scope  
25 of the present study.

26 Full ensemble distributions of mean latitudinal distributions of annual mean sea surface temperature (SST), with mean  
27 latitudinal distributions of maritime and continental surface air temperature in both DJF and JJA are plotted in Fig. 3,  
28 together with ensemble medians and 5% and 95% percentiles of global annual mean SST, and maritime surface air  
29 temperature in both DJF and JJA. The greater range of temperatures below rather than above median values reflects our use  
30 of a uniform range of CO<sub>2</sub> forcing values, and the logarithmic response of temperature to increasing CO<sub>2</sub> concentration.  
31 There is substantial variation of mean temperature across the ensemble, around 20 degrees over land, but the temperature

1 offset varies little with latitude outside of polar regions where snow and ice greatly reduce winter temperatures in the colder  
2 simulations. The variation in TPTD across the ensemble thus appears to be essentially driven by the strength of snow and ice  
3 albedo feedbacks.

4 Our ensemble distributions of sea and air temperatures are in broad agreement with the values from the Eocene model  
5 studies compared by Lunt et al. (2012), hereafter L12, and with the tables of marine and terrestrial proxy data compiled by  
6 L12Lunt et al. (2012) and HC11, covering the early Eocene, and including some records from the very latest Paleocene, but  
7 not including the PETM. Our palaeogeography specifically represents the early Eocene, but our range of CO<sub>2</sub> and orbital  
8 inputs is more representative of the variation in forcing across the whole era. L12 have summarised variations of SST with  
9 latitude from their proxy data set, in their Fig. 1, including large error bars representing uncertainty which they attribute to  
10 assumptions about seawater chemistry, possible non-analogous behaviour between modern and ancient systems, and  
11 uncertainty in calibrations of relationships between proxy data and properties of the palaeoclimate. Our median values of  
12 SST are close to the median estimates of SST in L12 at mid latitudes, and well within the uncertainty indicated by error bars  
13 at high latitudes.

14 Median values and standard deviations of precipitation at each grid cell are plotted in Fig. 4. Higher precipitation values and  
15 variation are largely confined to the tropics, especially to regions associated with monsoons in the present day: Africa and S.  
16 America in DJF, and S.E. Asia in JJA.

## 17 **4.2 Simple Metrics**

18 In Figs. 5 and 6, CO<sub>2</sub>, obliquity ( $\epsilon$ ) and precession index ( $\epsilon\sin\omega$ ) are plotted against MAT, northern seasonality, northern  
19 winter TPTD and northern summer TPTD (Fig. 5), and southern winter polar OLC, northern winter polar OLC, Asian  
20 monsoon index, African monsoon index and American monsoon index (Fig. 6). Subplots for obliquity and precession index  
21 in Figures 5 and 6 denote the CO<sub>2</sub> level on a continuous colour scale. The dominant effect of CO<sub>2</sub> on MAT and northern  
22 seasonality is apparent in Fig. 5, and it can also be seen that CO<sub>2</sub> strongly affects the northern TPTD in the winter, but not in  
23 the summer, when the combined influence of obliquity and precession index is discernible, suggesting that temperature  
24 proxies with seasonal bias may have a significant orbital imprint. The plot of atmospheric CO<sub>2</sub> against N. Winter TPTD  
25 shows a change in gradient at approximately 1000 ppm CO<sub>2</sub> and 32°C. This may be related to the logarithmic dependence of  
26 radiative forcing on CO<sub>2</sub> concentration, the disappearance of ice above some threshold level, and a minimum level of land  
27 surface albedo related to maximum vegetation cover. A possible sea ice related threshold mechanism influencing both SST  
28 and maritime air temperature in high northern latitudes may be observed in Fig. 3, and this is strongly associated with the  
29 increase in northern winter TPTD at low CO<sub>2</sub> levels. Zeebe et al. (2017) have analysed a high resolution benthic isotope  
30 record covering the late Palaeocene - early Eocene, and have concluded that orbitally paced cycles are unlikely to have been  
31 driven by high latitude mechanisms, but our PLASIM-GENIE modelling suggests that while northern TPTD is not orbitally  
32 paced in the winter, being controlled by CO<sub>2</sub>, it is orbitally paced in the summer, by a combination of obliquity and  
33 precession.

1 It can be observed in Fig. 6 that there is strong correlation between CO<sub>2</sub> and southern winter polar OLC. The African and  
2 Asian monsoon indices are both correlated with the precession index, a well established feature of Quaternary records (e.g.  
3 Cruz et al., 2005). The American monsoon index is fairly strongly correlated with the precession index at high levels of  
4 CO<sub>2</sub>, and negatively correlated with CO<sub>2</sub> at low levels of CO<sub>2</sub>. In each of the other examples, there is no apparent correlation  
5 between the simple metric and two of the three forcing factors. We have selected these simple metrics with visible  
6 correlations to the forcing parameters for further analysis with the linear modelling and emulation methods. Total effects on  
7 the simple metrics have been calculated for each of the forcing parameters, with eccentricity and precession considered  
8 separately, rather than combined within the precession index, and are shown in Table 4.

9 The total effects of CO<sub>2</sub> on MAT, northern winter TPTD and southern winter polar OLC, and of precession on both the  
10 Asian and African monsoon indices are all very high (> 0.90), and the total effects of obliquity on northern winter polar OLC  
11 and northern summer TPTD, are both fairly high (> 0.65), providing quantitative confirmation of the correlations visible in  
12 Figs. 5 and 6.

### 13 **4.3 Climate Sensitivity and Mean Air Temperature**

14 Figure 7 shows the relationship between CO<sub>2</sub> (plotted on a logarithmic scale), and MAT, with an abrupt change of gradient  
15 clearly visible at a CO<sub>2</sub> concentration of 1000 ppm. From the two gradients, we derive climate sensitivity values for a  
16 doubling of CO<sub>2</sub> concentration at CO<sub>2</sub> levels below 1000 ppm, and at CO<sub>2</sub> levels above 1000 ppm, of 4.36°C and 2.54°C  
17 respectively. We note that our modelled values of carbon in vegetation in the ENTS module remain low outside of the  
18 tropics at low CO<sub>2</sub> concentration, but as CO<sub>2</sub> concentration increases, land areas at higher latitudes reach maximum values of  
19 carbon in vegetation, with all land areas showing no further capacity for increased carbon in vegetation at an atmospheric  
20 concentration of ~1000 ppm. The increase in land vegetation cover, with corresponding reduction in albedo, acts as a  
21 positive feedback to rising temperature caused by increasing CO<sub>2</sub>, but this feedback mechanism ceases to operate when all  
22 available land is at its maximum vegetation capacity, with a consequent reduction in the climate sensitivity.

23 For a pre-industrial atmospheric CO<sub>2</sub> concentration of 280 ppm, the value of MAT indicated by our results for our early  
24 Eocene palaeogeography is 14.0°C. Holden et al. (2016) applied an identically configured PLASIM-GENIE to a modern  
25 geography, and their results show that with a pre-industrial CO<sub>2</sub> concentration, the model climate sensitivity is 3.8°C, and  
26 MAT is 12.9°C.

27 Our results also indicate values of global MAT for double, and four-times pre-industrial levels of CO<sub>2</sub> of 18.5°C and 22.5°C  
28 respectively; both these values are within the ranges of results for land near-surface air temperature in the modelling studies  
29 compared by L12, and shown in their Fig. 2b.

### 30 **4.4 Singular Value Decomposition**

31 Figure 8 shows the first three PCs of surface air temperature in DJF and JJA, with the percentages of temperature variation  
32 explained by each PC. Each of these plots illustrates the PC scaled by the standard deviation of the PC scores, thereby

1 reflecting the variability across the ensemble. Note the variable scales for each of the subplots. In both DJF and JJA, PC1  
2 explains over 95% of the variance, with TPTD clearly visible in both hemispheres in DJF, but apparent only in the southern  
3 hemisphere in JJA. OLC is apparent in the plots of PC1 in both DJF and JJA. OLC is discernible in PC2 for DJF  
4 temperature, which explains 2.4% of variance, but less apparent, at least in the southern hemisphere, for JJA temperatures, in  
5 which PC2 explains 2.6% of the variance. For temperature in both DJF and JJA, PC3 explains less than 1% of the variance,  
6 with some indication of TPTD and OLC in DJF, but only of weak OLC at high latitudes in JJA. It is worth noting that even  
7 though lower order PCs explain small percentages of global variances, these PCs are generally associated with specific  
8 regions where they are comparably important to the first PC.

9 In their presentation of the SVD method applied in this study, Holden et al. (2015) investigated the effects of orbital  
10 parameters on the Earth's climate in the present day, but without including CO<sub>2</sub> as a forcing parameter in their ensemble, and  
11 found that obliquity had a dominant effect on the PC score of annual average surface air temperature. In our study of the  
12 Eocene climate, CO<sub>2</sub> is strongly correlated with N. seasonality (Fig. 5), and obliquity is weakly correlated with TPTD in JJA  
13 (Fig. 5) and with OLC in DJF (Fig. 6). The first three PCs of precipitation in DJF and JJA are shown in Fig. 9. PC1 explains  
14 approximately 55% of the variance in both seasons, with PC2 and PC3 explaining over 20% and over 5% respectively, in  
15 both seasons. In both PC2 and PC3, areas of high seasonal contrast appear to correspond to areas which experience  
16 monsoons in the modern world.

17 Correlations between the PC scores of temperature and precipitation are provided in Table 5. The first PC scores of  
18 temperature, reflecting a global warming signal, are highly correlated with the first PC scores for precipitation, suggesting  
19 that these PCs reflect a strengthening of the hydrological cycle in response to warming. Similar considerations reveal  
20 connections between lower order PC scores, though we note that the 2<sup>nd</sup> (3<sup>rd</sup>) component of DJF temperature is associated  
21 with the 3<sup>rd</sup> (2<sup>nd</sup>) component of DJF precipitation. In order to address the drivers of these modes, we first consider the  
22 correlation coefficients,  $r$ , between forcing factors and the PC scores, shown in Table 6. These demonstrate that for each  
23 output there is a mode of variability driven by CO<sub>2</sub> and another mode driven by precession, suggesting they reflect global  
24 warming (and associated hydrological strength) and precessional forcing of the monsoon system.

25 There is strong correlation ( $r^2 > 0.5$ ) between CO<sub>2</sub> and the first PC scores of temperature in DJF and JJA. There are also  
26 strong correlations between precession index and the third PC scores for DJF temperature, and between precession index and  
27 the second PC scores for JJA temperature.

28 CO<sub>2</sub> is strongly correlated with the first PC scores of precipitation in both DJF and JJA, and there is a strong relationship  
29 between precession index and the second PC scores of precipitation in both DJF and JJA. An increase in the second PC  
30 scores for JJA precipitation in the Asian monsoon region (Fig. 9) corresponds to a decrease in the second PC scores for JJA  
31 temperature (Fig. 8), and as already noted, the second PC scores for both temperature and precipitation in JJA are strongly  
32 correlated to the precession index. This temperature reduction during the Asian monsoon was also observed by Holden et al.  
33 (2014), and attributed to a reduction in incoming solar radiation associated with increased cloud cover and surface  
34 evaporation.

## 1 4.5 Linear Modelling and Emulation

2 The relationships between the forcing parameters (with precession expressed as both  $\sin \omega$  and  $\cos \omega$ ) and the simple metrics,  
3 and between the forcing parameters and the PC scores of 2-D fields, derived through linear modelling, include first and  
4 second order terms of forcing factors, together with products of forcing factors. In all cases most of the main effects are  
5 confined to the first order terms, and in no case does eccentricity have a significant effect independently of either of the  
6 precession terms. All significant effects of the precession terms are accompanied by a small effect of eccentricity.

7 In Fig. 10, we plot the main effects of the forcing parameters on the first three PCs of temperature and precipitation for DJF.  
8 Figure 11 shows the main effects of the forcing parameters on the first three PCs of temperature and precipitation plotted for  
9 JJA.

10 In both seasons, PC1 for temperature and precipitation can be almost entirely explained by CO<sub>2</sub>, reinforcing the earlier  
11 conclusion that these describe a connected mode, global warming with associated effects on the hydrological cycle. The  
12 main effects also suggest connections between the modes of variability of temperature and precipitation in lower-order  
13 components. In both seasons, and apparent in both variables, there is a mode that is driven by precession; we interpret this  
14 as a monsoon signal, given precessional forcing and spatial patterns of rainfall that are characteristic of modern monsoons  
15 (Figs. 8 and 9). In JJA this is the second component of both variables. The mode is associated with precipitation variability  
16 of  $\sim 2.5$  mm/day and temperature variability of  $\sim 3^\circ\text{C}$ , with increased precipitation associated with a surface air cooling (note  
17 the negative correlation in Table 3, so that positive change in one field is associated with negative change in the other). In  
18 both cases, the local magnitude of variability is comparable to that driven by CO<sub>2</sub>. In DJF the precessional signal is again  
19 apparent in the second mode of precipitation, but the third mode of temperature. This mode is notable, in that it drives  
20 changes in simulated precipitation over East Africa (5 mm/day) that exceed CO<sub>2</sub>-driven variability. The remaining modes are  
21 more complex, and may not represent a clear mode of variability that can be straightforwardly attributed. For instance, the  
22 third-order mode of JJA temperature is driven by an interaction between CO<sub>2</sub> and obliquity, but in precipitation can be  
23 explained by a combination of precession and CO<sub>2</sub>.

24 All of the terms in the linear models derived from the forcing factors and the three monsoon indices are shown in Table 7.  
25 The Asian and African models are dominated by precession terms, roughly equally distributed between first order  $\sin(\omega)$  and  
26 the cross product of  $e$  and  $\sin(\omega)$ , with  $|\sin(\omega)|$  being approximately five times, and eight times larger than  $|\cos(\omega)|$  for the  
27 Asian and African models respectively. The American model identifies significant influence of CO<sub>2</sub>, in both the negative  
28 first order, and positive second order terms, with a similar magnitude of influence from combined precession terms, and with  
29  $|\sin(\omega)|$  being approximately three times larger than  $|\cos(\omega)|$ . All of the models have small contributions from first or second  
30 order, or cross products of  $\varepsilon$ , and from those terms of  $e$ , in addition to significant contributions from  $e\sin(\omega)$ . The terms in  
31 the models clearly reflect the relationships between the three monsoon indices and the two forcing factors CO<sub>2</sub> and  $e\sin(\omega)$   
32 shown in Fig. 6.

1 We apply these linear models as emulators to estimate values of monsoon indices corresponding to the full range of  
2 precession ( $\omega$ ), with eccentricity fixed at its high limit of 0.06, low and high values of CO<sub>2</sub> (300 ppm and 3000 ppm), and  
3 low and high values of obliquity (22.0° and 24.5°). Precession index ( $e\sin\omega$ ) and emulated values of the Asian, African and  
4 American monsoon indices for all four combinations of high and low CO<sub>2</sub> and obliquity are plotted in Figures 12, 13 and 14  
5 respectively. The elliptical form of each of the plots is controlled by model terms which include  $\cos(\omega)$ , and which identify  
6 seasonal processes in the development of the monsoons. Running each of the emulators with all of the terms in  $\cos(\omega)$   
7 excluded, generates points on a straight line between each apex of the ellipses generated by the full emulator. In each of the  
8 12 plots in Figs. 12-14,  $\omega$  increases anticlockwise from a value of 0° in the centre of the lower arc of the ellipse (with  
9 perihelion at the March equinox), through a value of 180° in the centre of the upper arc (with perihelion at the September  
10 equinox). Relationships between the precession index and the monsoon indices which are visually suggested in Figure 6 are  
11 shown with clear structure in Figures 12, 13 and 14. In each of the monsoon areas, the highest levels of precipitation occur  
12 when perihelion coincides with the summer solstice, in June for the Asian monsoon in the Northern Hemisphere, and in  
13 December for the African and American monsoons in the Southern Hemisphere. For the Asian and African monsoons,  
14 precipitation is increased by high CO<sub>2</sub>, particularly when perihelion is at the summer solstice, but for the American monsoon,  
15 high CO<sub>2</sub> decreases precipitation. The plots of the emulated African and American monsoons (Figs. 13 and 14) show the  
16 lowest and highest degrees of non-stationarity respectively, due to the relative magnitude of the  $\cos(\omega)$  terms in the linear  
17 models.

## 18 **5 Summary and Conclusions**

19 Our ensemble of 50 model runs of the EMIC PLASIM-GENIE has used an early Eocene palaeogeography incorporating  
20 recent understanding of the configuration of the continents and ocean gateways, with climate forcing by a randomly selected  
21 combination of atmospheric GHG emissions and orbital parameters for each model run. Relationships between forcing  
22 parameters and scalar summaries of model results have been derived through linear modelling.

23 Given the input range of CO<sub>2</sub>, our results show that, at the global scale, variability in patterns of surface air temperature is  
24 strongly dominated by a single mode of variation with a strong imprint of TPTD, focused in northern winter, that is entirely  
25 controlled by CO<sub>2</sub> (> 95% variance in both seasons). We note, however, that regions under the influence of monsoon  
26 systems exhibit precession-driven temperature variability that is comparable in magnitude to the variability driven by CO<sub>2</sub>  
27 (in large part the high proportion of variance explained by the CO<sub>2</sub> mode arises because the signal is global). In contrast to  
28 the unimodal dominance of CO<sub>2</sub> on the modelled global temperature fields, precipitation shows a somewhat more nuanced  
29 response. The first mode of precipitation, while still controlled entirely by CO<sub>2</sub>, is much less dominant (maximum 57%  
30 variance in DJF cf 21% for PC2). In the second and third spatial modes of precipitation variability, CO<sub>2</sub> is still important, but  
31 no more so than orbital parameters, with PC2 controlled more strongly by precession index.

1 The importance of orbital forcing to precipitation signals is seen more clearly in the OLC and monsoon indices. In spite of  
2 large variation in atmospheric CO<sub>2</sub>, variation in obliquity accounts for well over half of the variation in high northern latitude  
3 ocean-land temperature contrast, and the variation in precession is the dominant influence on seasonal variation in  
4 precipitation in tropical Africa and Asia, and combines with CO<sub>2</sub> to influence seasonal precipitation in tropical America. Our  
5 results strongly suggest the presence of monsoons in the early Eocene, but these climatic features would have developed  
6 without the effects of orography and high altitude plateau heating which are important factors in the modern south Asian  
7 monsoon (Boos and Kuang, 2010).

8 We note that the relative amplitude of the CO<sub>2</sub>-driven modes depends critically on the actual amplitude of CO<sub>2</sub> variability in  
9 the period of interest. While the ranges for orbital parameters are well defined, this is less true of CO<sub>2</sub> variability over the  
10 Eocene. If atmospheric CO<sub>2</sub> remained within a narrower range throughout the period, for example in the range 700 to 1800  
11 ppm, indicated for the early Eocene by Anagnostou et al. (2016) in a recent study using boron isotopes, then outside of short-  
12 lived hyperthermals, the relative influence of CO<sub>2</sub> and orbital inputs might have been more evenly balanced. Our modelling  
13 results suggest that climate sensitivity is state dependent, with a value of 4.36°C in a low CO<sub>2</sub> state, and 2.54°C in a high  
14 CO<sub>2</sub> state, due to a positive feedback mechanism in which albedo reduces as vegetation increases to its maximum value  
15 when CO<sub>2</sub> concentration reaches 1000 ppm.

16 We have demonstrated that emulators derived from linear modelling of the PLASIM-GENIE ensemble results can be used as  
17 a rapid and efficient method of estimating climate conditions from any set of forcing parameters, without the need for further  
18 deployment of the EMIC.

19 PLASIM-GENIE is to our knowledge the most sophisticated climate model that has been applied to an ensemble of Eocene  
20 simulations, but we note that increasing computing power is now enabling ensembles of simulations with moderately higher  
21 resolution models, such as HadCM3 (3.75° × 2.5°) (e.g. Araya-Melo et al., 2015; Lord et al., 2017), to be run, although with  
22 some limitation in the model years in each simulation. It will never be possible to apply state of the art climate models to  
23 large ensembles because, given the continual striving for the highest possible resolution, single simulations with such models  
24 will always be at the limits of what is practicable with available computing power. EMICs therefore have an important role  
25 in furthering our understanding of past, present and future climate systems, and in the rapid identification of influencing  
26 factors and modes of response which may be targeted for study by slower but more powerful models.

27 Our study of the early Eocene climate and the PETM using PLASIM-GENIE has shown that variability in orbital parameters  
28 can exert significant climatic influence, particularly in regard to tropical temperature and precipitation, and they should not  
29 be ignored in modelling studies of climates of the past.

## 30 **Data Availability**

31 Details on access to the model code, and instructions on compiling the model are given in Holden et al. (2016).

## 1 **Appendix A Hypercube Generation**

2 This study has been designed together with a future study using the EMIC model GENIE-1 (Edwards and Marsh, 2005).  
3 The GENIE-1 model will use all four of the forcing parameters and the dummy parameter, used in the present study, together  
4 with an additional six forcing parameters not used by the PLASIM-GENIE study. For PLASIM-GENIE we have run 50  
5 simulations with five parameters, while in GENIE-1 we will run 100 simulations with 11 parameters, so that the number of  
6 runs in each ensemble is approximately 10 times the input dimension (Loeppky et al., 2012).

7 The overall design for both studies is based on a maximin Latin hypercube with 100 rows and 11 columns produced by  
8 repeatedly invoking the lhsdesign function in MATLAB (MathWorks), with the command:

```
9 hyperCube = lhsdesign(100, 11, 'criterion', 'maximin', 'iterations', 100);
```

10 to select from 100 iteratively generated hypercubes, the one which best fits the maximin criterion, i.e. where the minimum  
11 Euclidian distance between points in hyperspace is at a maximum. This MATLAB command is repeated until the absolute  
12 value of correlation between columns falls below a selected value, or until a selected number of attempts has been made.  
13 The ability of this ‘brute force’ approach to produce a hypercube which satisfies the maximin criterion, with the required low  
14 correlation between columns decreases rapidly with an increasing number of columns, and a decreasing target correlation,  
15 but in several minutes it can generate a hypercube with 100 rows, each representing a design point for an ensemble member,  
16 and 11 columns, each representing a forcing or dummy parameter, with correlation between any two parameters not  
17 exceeding 0.1.

18 We then modify the overall design by first picking a subset of 50 of the 100 design points to give good coverage of the  
19 PLASIM-GENIE subspace. We randomly select an initial point, and iteratively select from the remainder, without  
20 replacement, the point which provides the largest increase in the number of populated sectors across all the two-dimensional  
21 projections of PLASIM-GENIE parameter space defined by dividing each two-dimensional subspace into 6 x 6 equal  
22 sectors.

23 This defines a template comprising a 50-member subset of 11 parameter values.

24 Copying the template and discarding the six parameters which are only used in the GENIE-1 ensemble yields the final  
25 hypercube design for the PLASIM-GENIE ensemble, comprising 50 sets of five parameters.

26 A second copy of the template forms the top half of the GENIE-1 hypercube, and the bottom half is partially constructed by  
27 duplicating only the five PLASIM-GENIE parameters from the first 50 rows, with the remaining six parameters determined  
28 by choosing a previously unselected point, without replacement, from the initial 100 x 11 hypercube that maximises the  
29 Euclidean distance between the pair of points in the subspace of the remaining six parameters.

30 Following this procedure, the two hypercubes for the PLASIM-GENIE and GENIE-1 studies both show very good state-  
31 space coverage and low correlation, and each member of the PLASIM-GENIE ensemble has two corresponding members in

1 the GENIE-1 ensemble, with identical values for the parameters in common, but widely differing sets of values for the  
2 parameters only used by GENIE-1.

### 3 **Author Contribution**

4 J. Keery and P. Holden designed and prepared the ensemble configurations and analysed the model outputs with advice from  
5 N. Edwards. J. Keery prepared the manuscript with contributions from both co-authors.

### 6 **Competing Interests**

7 The authors declare that they have no conflict of interest.

### 8 **Acknowledgements**

9 The authors gratefully acknowledge support from NERC, with funding for project NE/K006223/1. We are very grateful to  
10 the reviewers M. Crucifix and D. De Vleeschouwer, and to the editor A. Winguth, for their thorough and constructive  
11 comments which have helped to improve the manuscript.

### 12 **References**

- 13 Abbot, D. S. and Tziperman, E.: A high-latitude convective cloud feedback and equable climates, *Q. J. Roy. Meteor. Soc.*,  
14 134, 165-185, doi.10.1002/qj.211, 2008
- 15 Akaike, H.: A new look at the statistical model identification, *IEEE transactions on automatic control*, 19, 716-723, 1974
- 16 Akhmetiev, M. A., Zaporozhets, N. I., Benyamovskiy, V. N., Aleksandrova, G. N., Iakovleva, A. I., and Oreshkina, T. V.:  
17 The Paleogene history of the Western Siberian seaway - A connection of the Peri-Tethys to the Arctic Ocean, *Austrian J.*  
18 *Earth Sci.*, 105, 50-67, 2012
- 19 Anagnostou, E., John, E. H., Edgar, K. M., Foster, G. L., Ridgwell, A., Inglis, G. N., Pancost, R. D., Lunt, D. J., and  
20 Pearson, P. N.: Changing atmospheric CO<sub>2</sub> concentration was the primary driver of early Cenozoic climate, *Nature*, 533,  
21 380-384, doi.10.1038/nature17423, 2016
- 22 Araya-Melo, P. A., Crucifix, M., and Bounceur, N.: Global sensitivity analysis of the Indian monsoon during the  
23 Pleistocene, *Clim. Past*, 11, 45, doi.10.5194/cp-11-45-2015, 2015
- 24 Aubry, M.-P., Ouda, K., Dupuis, C., Berggren, W. A., and Couvering, J. A. V.: The Global Standard Stratotype-section and  
25 Point (GSSP) for the base of the Eocene Series in the Dababiya section (Egypt), *Episodes*, 30, 271, 2007

1 Backman, J., Jakobsson, M., Frank, M., Sangiorgi, F., Brinkhuis, H., Stickley, C., O'Regan, M., Løvlie, R., Pälike, H.,  
2 Spofforth, D., Gattacecca, J., Moran, K., King, J., and Heil, C.: Age model and core-seismic integration for the Cenozoic  
3 Arctic Coring Expedition sediments from the Lomonosov Ridge, *Paleoceanography*, 23, doi.10.1029/2007PA001476, 2008  
4 Barker, P. and Burrell, J.: The opening of Drake passage, *Mar. Geol.*, 25, 15-34, 1977  
5 Berger, A., Loutre, M. F., and Tricot, C.: Insolation and Earth's orbital periods, *J. Geophys. Res.-Atmos.*, 98, 10341-10362,  
6 1993  
7 Boos, W. R. and Kuang, Z.: Dominant control of the South Asian monsoon by orographic insulation versus plateau heating,  
8 *Nature*, 463, 218-222, doi.10.1038/nature08707, 2010  
9 Bounceur, N., Crucifix, M., and Wilkinson, R.: Global sensitivity analysis of the climate–vegetation system to astronomical  
10 forcing: an emulator-based approach, *Earth System Dynamics*, 6, 205-224, doi.10.5194/esd-6-205-2015, 2015  
11 Burnham, K. P. and Anderson, D. R.: *Model selection and multimodel inference: a practical information-theoretic approach*,  
12 Springer, New York, 2003.  
13 Carmichael, M. J., Lunt, D. J., Huber, M., Heinemann, M., Kiehl, J., LeGrande, A., Loftson, C. A., Roberts, C. D., Sagoo,  
14 N., Shields, C., Valdes, P. J., Winguth, A., Winguth, C., and Pancost, R. D.: A model–model and data–model comparison for  
15 the early Eocene hydrological cycle, *Clim. Past*, 12, 455-481, doi.10.5194/cp-12-455-2016, 2016  
16 Chen, Z., Ding, Z., Yang, S., Zhang, C., and Wang, X.: Increased precipitation and weathering across the Paleocene-Eocene  
17 thermal maximum in central China, *Geochem. Geophys. Geosy.*, 17, 2286–2297, doi.10.1002/2016GC006333, 2016  
18 Cruz, F. W., Burns, S. J., Karmann, I., Sharp, W. D., Vuille, M., Cardoso, A. O., Ferrari, J. A., Silva Dias, P. L., and Viana,  
19 O.: Insolation-driven changes in atmospheric circulation over the past 116,000 years in subtropical Brazil, *Nature*, 434, 63-  
20 66, doi.10.1038/nature03365, 2005  
21 Cui, Y., Kump, L. R., Ridgwell, A. J., Charles, A. J., Junium, C. K., Diefendorf, A. F., Freeman, K. H., Urban, N. M., and  
22 Harding, I. C.: Slow release of fossil carbon during the Palaeocene-Eocene Thermal Maximum, *Nat. Geosci.*, 4, 481-485,  
23 doi.10.1038/NGEO1179, 2011  
24 Dickens, G. R.: Down the rabbit hole: Toward appropriate discussion of methane release from gas hydrate systems during  
25 the Paleocene-Eocene thermal maximum and other past hyperthermal events, *Clim. Past*, 7, 831-846, doi.10.5194/cp-7-831-  
26 2011, 2011  
27 Dickson, A. J., Cohen, A. S., and Coe, A. L.: Seawater oxygenation during the Paleocene-Eocene thermal maximum,  
28 *Geology*, 40, 639-642, doi.10.1130/G32977.1, 2012  
29 Dunkley Jones, T., Lunt, D. J., Schmidt, D. N., Ridgwell, A., Sluijs, A., Valdes, P. J., and Maslin, M.: Climate model and  
30 proxy data constraints on ocean warming across the Paleocene–Eocene Thermal Maximum, *Earth-Sci. Rev.*, 125, 123-145,  
31 doi.10.1016/j.earscirev.2013.07.004, 2013  
32 Edwards, N. R. and Marsh, R.: Uncertainties due to transport-parameter sensitivity in an efficient 3-D ocean-climate model,  
33 *Clim. Dynam.*, 24, 415-433, doi.10.1007/s00382-004-0508-8, 2005

1 Exon, N. F., Kennett, J. P., and Malone, M. J.: Leg 189 synthesis: Cretaceous–Holocene history of the Tasmanian Gateway.  
2 In: Proceedings of the Ocean Drilling Program, Scientific Results, 189, Exon, N. F., Kennett, J. P., and Malone, M. J. (Eds.),  
3 Ocean Drilling Program, College Station, TX 2004.

4 Fraedrich, K.: A suite of user-friendly global climate models: hysteresis experiments, *Eur. Phys. J. Plus*, 127, 1-9,  
5 doi.10.1140/epjp/i2012-12053-7, 2012

6 Fraedrich, K., Kirk, E., Luksch, U., and Lunkeit, F.: The portable university model of the atmosphere (PUMA): Storm track  
7 dynamics and low-frequency variability, *Meteorol. Z.*, 14, 735-745, doi.10.1127/0941-2948/2005/0074, 2005

8 Gehler, A., Gingerich, P. D., and Pack, A.: Temperature and atmospheric CO<sub>2</sub> concentration estimates through the PETM  
9 using triple oxygen isotope analysis of mammalian bioapatite, *P. Natl. Acad. Sci. USA*, doi: 10.1073/pnas.1518116113,  
10 2016. 201518116, doi.10.1073/pnas.1518116113, 2016

11 Gibbs, S. J., Bown, P. R., Sessa, J. A., Bralower, T. J., and Wilson, P. A.: Nannoplankton extinction and origination across  
12 the Paleocene-Eocene thermal maximum, *Science*, 314, 1770-1773, 2006

13 Hannachi, A.: A primer for EOF analysis of climate data. University of Reading, Reading, 2004.

14 Herold, N., Buzan, J., Seton, M., Goldner, A., Green, J., Müller, R., Markwick, P., and Huber, M.: A suite of early Eocene (~  
15 55 Ma) climate model boundary conditions, *Geosci. Model Dev.*, 7, 2077-2090, doi.10.5194/gmd-7-2077-2014, 2014

16 Hibler III, W.: A dynamic thermodynamic sea ice model, *J. Phys. Oceanogr.*, 9, 815-846, 1979

17 Hilgen, F. J., Kuiper, K. F., and Lourens, L. J.: Evaluation of the astronomical time scale for the Paleocene and earliest  
18 Eocene, *Earth Planet. Sc. Lett.*, 300, 139-151, doi.10.1016/j.epsl.2010.09.044, 2010

19 Hinnov, L. A. and Hilgen, F. J.: Chapter 4 - Cyclostratigraphy and Astrochronology. In: *The Geologic Time Scale 2012*,  
20 Gradstein, F. M., Ogg, J. G., Schmitz, M. D., and Ogg, G. M. (Eds.), Elsevier, Boston, 2012.

21 Holden, P., Edwards, N., Garthwaite, P., Fraedrich, K., Lunkeit, F., Kirk, E., Labriet, M., Kanudia, A., and Babonneau, F.:  
22 PLASIM-ENTSem v1. 0: a spatio-temporal emulator of future climate change for impacts assessment, *Geosci. Model Dev.*,  
23 7, 433-451, doi.10.5194/gmd-7-433-2014, 2014

24 Holden, P. B., Edwards, N. R., Fraedrich, K., Kirk, E., Lunkeit, F., and Zhu, X.: PLASIM–GENIE v1.0: a new intermediate  
25 complexity AOGCM, *Geosci. Model Dev.*, 9, 3347-3361, doi.10.5194/gmd-9-3347-2016, 2016

26 Holden, P. B., Edwards, N. R., Garthwaite, P. H., and Wilkinson, R. D.: Emulation and interpretation of high-dimensional  
27 climate model outputs, *J. Appl. Stat.*, 42, 2038-2055, doi.10.1080/02664763.2015.1016412, 2015

28 Homma, T. and Saltelli, A.: Importance measures in global sensitivity analysis of nonlinear models, *Reliability Engineering  
29 and System Safety*, 52, 1-17, 1996

30 Huber, M.: Progress in greenhouse climate modeling. In: *Reconstructing Earth’s Deep-Time Climate - The State of the Art  
31 in 2012*, Ivany, L. C. and Huber, B. T. (Eds.), The Paleontological Society, Boulder, CO, 2012.

32 Huber, M. and Caballero, R.: The early Eocene equable climate problem revisited, *Clim. Past*, 7, 603-633, doi.10.5194/cp-7-  
33 603-2011, 2011

1 Jain, S., Lall, U., and Mann, M. E.: Seasonality and interannual variations of Northern Hemisphere temperature: Equator-to-  
2 pole gradient and ocean-land contrast, *J. Climate*, 12, 1086-1100, 1999

3 Jenkyns, H. C.: Geochemistry of oceanic anoxic events, *Geochem. Geophys. Geosy.*, 11, doi.10.1029/2009GC002788, 2010

4 Jones, P. D. and Mann, M. E.: Climate over past millennia, *Rev. Geophys.*, 42, 2004

5 Karoly, D. J. and Braganza, K.: Identifying global climate change using simple indices, *Geophys. Res. Lett.*, 28, 2205-2208,  
6 2001

7 Kennett, J. and Stott, L.: Abrupt deep-sea warming, palaeoceanographic changes and benthic extinctions at the end of the  
8 Palaeocene, *Nature*, 353, 225-229, doi.10.1038/353225a0, 1991

9 Laskar, J., Fienga, A., Gastineau, M., and Manche, H.: La2010: a new orbital solution for the long-term motion of the Earth,  
10 *Astron. Astrophys.*, 532, A89, doi.10.1051/0004-6361/201116836, 2011

11 Lauretano, V., Littler, K., Polling, M., Zachos, J. C., and Lourens, L. J.: Frequency, magnitude and character of  
12 hyperthermal events at the onset of the Early Eocene Climatic Optimum, *Clim. Past*, 11, 1313-1324, doi.10.5194/cp-11-  
13 1313-2015, 2015

14 Laurin, J., Meyers, S. R., Galeotti, S., and Lanci, L.: Frequency modulation reveals the phasing of orbital eccentricity during  
15 Cretaceous Oceanic Anoxic Event II and the Eocene hyperthermals, *Earth Planet. Sc. Lett.*, 442, 143-156,  
16 doi.10.1016/j.epsl.2016.02.047, 2016

17 Loepky, J. L., Sacks, J., and Welch, W. J.: Choosing the sample size of a computer experiment: A practical guide,  
18 *Technometrics*, 2012. 2012

19 Lord, N. S., Crucifix, M., Lunt, D. J., Thorne, M. C., Bounceur, N., Dowsett, H., O'Brien, C. L., and Ridgwell, A.:  
20 Emulation of long-term changes in global climate: Application to the late Pliocene and future, *Clim. Past*, 2017, 1-47,  
21 doi.10.5194/cp-2017-57, 2017

22 Lourens, L. J., Sluijs, A., Kroon, D., Zachos, J. C., Thomas, E., Röhl, U., Bowles, J., and Raffi, I.: Astronomical pacing of  
23 late Palaeocene to early Eocene global warming events, *Nature*, 435, 1083-1087, doi.10.1038/nature03814, 2005

24 Lunt, D., Elderfield, H., Pancost, R., Ridgwell, A., Foster, G., Haywood, A., Kiehl, J., Sago, N., Shields, C., and Stone, E.:  
25 Warm climates of the past—a lesson for the future?, *Philos. T. R. Soc.-A*, 371, 20130146, doi.10.1098/rsta.2013.0146, 2013

26 Lunt, D. J., Dunkley Jones, T., Heinemann, M., Huber, M., LeGrande, A., Winguth, A., Loftson, C., Marotzke, J., Roberts,  
27 C., and Tindall, J.: A model–data comparison for a multi-model ensemble of early Eocene atmosphere–ocean simulations:  
28 EoMIP, *Clim. Past*, 8, 1717-1736, doi.10.5194/cp-8-1717-2012, 2012

29 Lunt, D. J., Farnsworth, A., Loftson, C., Foster, G. L., Markwick, P., O'Brien, C. L., Pancost, R. D., Robinson, S. A., and  
30 Wrobel, N.: Palaeogeographic controls on climate and proxy interpretation, *Clim. Past*, 12, 1181-1198, doi.10.5194/cp-12-  
31 1181-2016, 2016

32 Lunt, D. J., Huber, M., Anagnostou, E., Baatsen, M. L. J., Caballero, R., DeConto, R., Dijkstra, H. A., Donnadieu, Y.,  
33 Evans, D., Feng, R., Foster, G. L., Gasson, E., von der Heydt, A. S., Hollis, C. J., Inglis, G. N., Jones, S. M., Kiehl, J.,  
34 Kirtland Turner, S., Korty, R. L., Kozdon, R., Krishnan, S., Ladant, J. B., Langebroek, P., Lear, C. H., LeGrande, A. N.,

1 Littler, K., Markwick, P., Otto-Bliesner, B., Pearson, P., Poulsen, C. J., Salzmann, U., Shields, C., Snell, K., Stürz, M.,  
2 Super, J., Tabor, C., Tierney, J. E., Tourte, G. J. L., Tripathi, A., Upchurch, G. R., Wade, B. S., Wing, S. L., Winguth, A. M.  
3 E., Wright, N. M., Zachos, J. C., and Zeebe, R. E.: The DeepMIP contribution to PMIP4: experimental design for model  
4 simulations of the EECO, PETM, and pre-PETM (version 1.0), *Geosci. Model Dev.*, 10, 889-901, doi.10.5194/gmd-10-889-  
5 2017, 2017

6 Lunt, D. J., Ridgwell, A., Sluijs, A., Zachos, J., Hunter, S., and Haywood, A.: A model for orbital pacing of methane hydrate  
7 destabilization during the Palaeogene, *Nat. Geosci.*, 4, 775-778, doi.10.1038/ngeo1266, 2011

8 Marinovich, L., Brouwers, E. M., Hopkins, D. M., and McKenna, M. C.: Late Mesozoic and Cenozoic paleogeographic and  
9 paleoclimatic history of the Arctic Ocean Basin, based on shallow-water faunas and terrestrial vertebrates. In: *The Geology*  
10 *of North America, L: The Arctic Ocean Region*, Grantz, A., Sweeney, J. F., and Johnson, G. L. (Eds.), Geological Society of  
11 America, 1990.

12 Marsh, R., Müller, S., Yool, A., and Edwards, N.: Incorporation of the C-GOLDSTEIN efficient climate model into the  
13 GENIE framework: "eb\_go\_gs" configurations of GENIE, *Geosci. Model Dev.*, 4, 957-992, doi.10.5194/gmd-4-957-2011,  
14 2011

15 MathWorks: <https://uk.mathworks.com/help/stats/lhsdesign.html>, last access: 17 August 2017.

16 McInerney, F. A. and Wing, S. L.: The Paleocene-Eocene Thermal Maximum: A perturbation of carbon cycle, climate, and  
17 biosphere with implications for the future, *Annu. Rev. Earth Pl. Sc.*, 39, 489-516, doi.10.1146/annurev-earth-040610-  
18 133431, 2011

19 McKay, M. D., Beckman, R. J., and Conover, W. J.: A comparison of three methods for selecting values of input variables in  
20 the analysis of output from a computer code, *Technometrics*, 21, 239-245, 1979

21 O'Regan, M., Moran, K., Backman, J., Jakobsson, M., Sangiorgi, F., Brinkhuis, H., Pockalny, R., Skelton, A., Stickley, C.,  
22 and Koç, N.: Mid-Cenozoic tectonic and paleoenvironmental setting of the central Arctic Ocean, *Paleoceanography*, 23,  
23 doi.10.1029/2007PA001559, 2008

24 Oakley, J. E. and O'Hagan, A.: Probabilistic sensitivity analysis of complex models: a Bayesian approach, *Journal of the*  
25 *Royal Statistical Society: Series B (Statistical Methodology)*, 66, 751-769, 2004

26 Peixoto, J. P. and Oort, A. H.: *Physics of Climate*, American Institute of Physics, New York, 1992.

27 Penman, D. E.: Silicate weathering and North Atlantic silica burial during the Paleocene-Eocene Thermal Maximum,  
28 *Geology*, doi: 10.1130/G37704.1, 2016. G37704. 37701, doi.10.1130/G37704.1, 2016

29 Penman, D. E., Hönlisch, B., Zeebe, R. E., Thomas, E., and Zachos, J. C.: Rapid and sustained surface ocean acidification  
30 during the Paleocene-Eocene Thermal Maximum, *Paleoceanography*, 29, 357-369, doi.10.1002/2014PA002621, 2014

31 Radionova, E. and Khokhlova, I.: Was the North Atlantic connected with the Tethys via the Arctic in the early Eocene?  
32 Evidence from siliceous plankton, *GFF*, 122, 133-134, doi.10.1080/11035890001221133, 2000

33 Rougier, J.: Probabilistic inference for future climate using an ensemble of climate model evaluations, *Climatic Change*, 81,  
34 247-264, doi.10.1007/s10584-006-9156-9, 2007

1 Schwarz, G.: Estimating the dimension of a model, *The annals of statistics*, 6, 461-464, 1978

2 Semtner Jr, A. J.: A model for the thermodynamic growth of sea ice in numerical investigations of climate, *J. Phys.*  
3 *Oceanogr.*, 6, 379-389, 1976

4 Sexton, P. F., Norris, R. D., Wilson, P. A., Pälike, H., Westerhold, T., Röhl, U., Bolton, C. T., and Gibbs, S.: Eocene global  
5 warming events driven by ventilation of oceanic dissolved organic carbon, *Nature*, 471, 349-352, doi.10.1038/nature09826,  
6 2011

7 Sijp, W. P., Anna, S., Dijkstra, H. A., Flögel, S., Douglas, P. M., and Bijl, P. K.: The role of ocean gateways on cooling  
8 climate on long time scales, *Global Planet. Change*, 119, 1-22, doi.10.1016/j.gloplacha.2014.04.004, 2014

9 Slattery, J. S., Cobban, W. A., McKinney, K. C., Harries, P. J., and Sandness, A. L.: Early Cretaceous to Paleocene  
10 paleogeography of the Western Interior Seaway: The interaction of eustasy and tectonism. In: *Cretaceous Conference:*  
11 *Evolution and Revolution*, Bingle-Davis, M. (Ed.), Wyoming Geological Association, Casper, WY, 2015.

12 Sloan, L. C. and Barron, E. J.: "Equable" climates during Earth history?, *Geology*, 18, 489-492, 1990

13 Sluijs, A., Schouten, S., Pagani, M., Woltering, M., Brinkhuis, H., Damsté, J. S. S., Dickens, G. R., Huber, M., Reichert, G.-  
14 J., and Stein, R.: Subtropical Arctic Ocean temperatures during the Palaeocene/Eocene thermal maximum, *Nature*, 441, 610-  
15 613, doi.10.1038/nature04668, 2006

16 Sluijs, A., Zachos, J. C., and Zeebe, R. E.: Constraints on hyperthermals, *Nat. Geosci.*, 5, 231-231, doi.10.1038/ngeo1423,  
17 2012

18 Smith, M. E., Carroll, A. R., Scott, J. J., and Singer, B. S.: Early Eocene carbon isotope excursions and landscape  
19 destabilization at eccentricity minima: Green River Formation of Wyoming, *Earth Planet. Sc. Lett.*, 403, 393-406,  
20 doi.10.1016/j.epsl.2014.06.024, 2014

21 Thomas, D. J., Zachos, J. C., Bralower, T. J., Thomas, E., and Bohaty, S.: Warming the fuel for the fire: Evidence for the  
22 thermal dissociation of methane hydrate during the Paleocene-Eocene thermal maximum, *Geology*, 30, 1067-1070, 2002

23 Trenberth, K. E., Hurrell, J. W., and Stepaniak, D. P.: The Asian monsoon: Global perspectives. In: *The Asian Monsoon*,  
24 Wang, B. (Ed.), Springer, New York, 2006.

25 Wang, B. and Fan, Z.: Choice of South Asian summer monsoon indices, *B. Am. Meteorol. Soc.*, 80, 629, 1999

26 Weber, S. L.: The utility of Earth system Models of Intermediate Complexity (EMICs), *Wiley Interdisciplinary Reviews:*  
27 *Climate Change*, 1, 243-252, doi.10.1002/wcc.24, 2010

28 Westerhold, T., Röhl, U., and Laskar, J.: Time scale controversy: Accurate orbital calibration of the early Paleogene,  
29 *Geochem. Geophys. Geosy.*, 13, doi.10.1029/2012GC004096, 2012

30 Westerhold, T., Röhl, U., McCarren, H. K., and Zachos, J. C.: Latest on the absolute age of the Paleocene–Eocene Thermal  
31 Maximum (PETM): new insights from exact stratigraphic position of key ash layers+ 19 and– 17, *Earth Planet. Sc. Lett.*,  
32 287, 412-419, doi.10.1016/j.epsl.2009.08.027, 2009

33 Williamson, M. S., Lenton, T. M., Shepherd, J. G., and Edwards, N. R.: An efficient numerical terrestrial scheme (ENTS) for  
34 Earth system modelling, *Ecol. Model.*, 198, 362-374, doi.10.1016/j.ecolmodel.2006.05.027, 2006

- 1 Wing, S. L. and Greenwood, D. R.: Fossils and fossil climate: the case for equable continental interiors in the Eocene,  
2 Philos. T. R. Soc.-B, 341, 243-252, 1993
- 3 Wyss, G. D. and Jorgensen, K. H.: A User's Guide to LHS: Sandia's Latin Hypercube Sampling Software. Sandia National  
4 Laboratories, Albuquerque, NM, 1998.
- 5 Zachos, J. C., Bohaty, S. M., John, C. M., McCarren, H., Kelly, D. C., and Nielsen, T.: The Palaeocene–Eocene carbon  
6 isotope excursion: constraints from individual shell planktonic foraminifer records, Philos. T. R. Soc.-A, 365, 1829-1842,  
7 doi.10.1098/rsta.2007.2045, 2007
- 8 Zachos, J. C., Röhl, U., Schellenberg, S. A., Sluijs, A., Hodell, D. A., Kelly, D. C., Thomas, E., Nicolo, M., Raffi, I.,  
9 Lourens, L. J., McCarren, H., and Kroon, D.: Rapid Acidification of the Ocean during the Paleocene-Eocene Thermal  
10 Maximum, Science, 308, 1611-1615, doi.10.2307/3841617, 2005
- 11 Zachos, J. C., Wara, M. W., Bohaty, S., Delaney, M. L., Petrizzo, M. R., Brill, A., Bralower, T. J., and Premoli-Silva, I.: A  
12 transient rise in tropical sea surface temperature during the Paleocene-Eocene thermal maximum, Science, 302, 1551-1554,  
13 2003
- 14 Zeebe, R. E., Ridgwell, A., and Zachos, J. C.: Anthropogenic carbon release rate unprecedented during the past 66 million  
15 years, Nat. Geosci., 9, 325–329, doi.10.1038/ngeo2681, 2016
- 16 Zeebe, R. E. and Zachos, J. C.: Long-term legacy of massive carbon input to the Earth system: Anthropocene versus Eocene,  
17 Philos. T. R. Soc.-A, 371, 20120006, doi.10.1098/rsta.2012.0006, 2013
- 18  
19

20 **Table 1** Uniform ranges for forcing and dummy parameters

	min	max
<b>pCO<sub>2</sub> (ppm)</b>	280	3000
<b>Precession (°)</b>	0	360
<b>Obliquity (°)</b>	22.0	24.5
<b>Eccentricity (-)</b>	0.00	0.06
<b>Dummy (-)</b>	0	1

21

22 **Table 2** Forcing factors and dummy values for each member in the ensemble. Precession =  $\omega$ , the angle between the  
23 moving vernal equinox and the longitude of perihelion.

Member (-)	CO <sub>2</sub> (ppm)	Eccentricity (-)	Precession (°)	Obliquity (°)	Dummy (-)
1	975.6	0.0022	142.5	22.37	0.822
2	2418.7	0.0256	165.2	23.95	0.907
3	1259.4	0.0007	307.1	23.91	0.323
4	801.3	0.0163	270.4	23.50	0.276
5	1720.1	0.0559	206.7	23.82	0.402
6	327.1	0.0595	135.9	23.53	0.681

7	2937.7	0.0418	287.1	22.53	0.650
8	1200.3	0.0237	313.2	24.12	0.978
9	1420.7	0.0158	297.1	23.86	0.931
10	2157.6	0.0432	100.6	23.74	0.661
11	1791.7	0.0241	247.2	23.43	0.429
12	2369.0	0.0425	78.9	22.65	0.167
13	2502.9	0.0296	0.5	22.69	0.122
14	2149.2	0.0405	249.9	24.23	0.347
15	1061.7	0.0394	40.9	23.94	0.189
16	711.3	0.0199	274.6	22.08	0.913
17	1817.1	0.0578	291.4	23.08	0.888
18	722.1	0.0463	195.8	24.38	0.865
19	2988.5	0.0039	110.1	24.40	0.049
20	539.4	0.0251	212.5	23.29	0.234
21	450.6	0.0335	96.1	22.28	0.674
22	2700.1	0.0049	165.9	23.66	0.630
23	2025.4	0.0320	189.4	23.63	0.087
24	2268.7	0.0308	233.3	22.86	0.461
25	1447.2	0.0364	62.0	23.40	0.541
26	1168.3	0.0300	147.4	22.97	0.947
27	1317.6	0.0377	12.4	23.04	0.714
28	1639.5	0.0265	150.9	22.98	0.524
29	399.0	0.0589	262.7	23.46	0.028
30	2876.3	0.0411	203.0	22.05	0.608
31	2611.1	0.0170	54.3	22.84	0.746
32	2831.7	0.0564	187.2	23.72	0.696
33	1998.5	0.0372	278.8	24.19	0.805
34	1465.0	0.0439	38.9	23.50	0.376
35	1660.0	0.0109	85.3	22.88	0.896
36	2393.7	0.0587	127.9	24.27	0.191
37	286.3	0.0004	27.1	23.99	0.391
38	667.4	0.0509	116.5	22.71	0.569
39	2246.8	0.0450	317.4	22.90	0.103
40	2334.2	0.0096	294.7	23.61	0.532
41	2968.2	0.0346	329.8	22.51	0.314
42	768.2	0.0085	218.3	23.00	0.000
43	925.8	0.0450	327.2	24.32	0.753
44	384.5	0.0081	60.6	22.59	0.436
45	850.7	0.0551	322.9	23.21	0.459
46	1112.8	0.0150	356.7	23.27	0.579
47	1255.8	0.0116	212.2	22.31	0.487
48	1124.1	0.0530	343.7	22.40	0.065
49	2113.9	0.0276	9.9	22.19	0.856
50	1681.0	0.0354	175.5	22.45	0.287

1  
2  
3

1 **Table 3** **R<sup>2</sup> correlation between PC scores from SVD and PC scores emulated with the linear models.**

	<b>PC1</b>	<b>PC2</b>	<b>PC3</b>
<b>DJF_temperature</b>	0.95	0.58	0.75
<b>JJA_temperature</b>	0.97	0.97	0.72
<b>DJF_precipitation</b>	0.97	0.92	0.64
<b>JJA_precipitation</b>	0.99	0.99	0.89

2

3

4 **Table 4** **Total effects of forcing parameters on simple scalar metrics.**

	<b>CO<sub>2</sub></b>	<b>Eccentricity</b>	<b>Obliquity</b>	<b>Precession</b>
<b>MAT</b>	0.993	0.002	0.000	0.005
<b>N. seasonality</b>	0.766	0.003	0.011	0.220
<b>N. winter TPTD</b>	0.939	0.006	0.039	0.017
<b>N. summer TPTD</b>	0.144	0.000	0.673	0.183
<b>S. winter POLC</b>	0.979	0.004	0.005	0.012
<b>N. winter POLC</b>	0.088	0.000	0.789	0.122
<b>Asian monsoon index</b>	0.094	0.004	0.063	0.840
<b>African monsoon index</b>	0.017	0.001	0.001	0.981
<b>American monsoon index</b>	0.490	0.004	0.020	0.486

5

1 Table 5 R correlation values for PC scores for temperature and precipitation in DJF and JJA. Values where  $R^2 \geq 0.5$   
 2 are shown in red.

		DJF_precipitation		
		PC1	PC2	PC3
DJF_temperature	PC1	<b>0.993</b>	-0.004	-0.080
	PC2	-0.067	-0.364	<b>-0.864</b>
	PC3	0.005	<b>0.783</b>	-0.354
		JJA_precipitation		
		PC1	PC2	PC3
JJA_temperature	PC1	<b>0.976</b>	0.091	0.157
	PC2	0.098	<b>-0.947</b>	0.082
	PC3	-0.180	-0.049	<b>0.795</b>

3

4

5 Table 6 R correlation values for forcing factors and PC scores. Values where  $R^2 \geq 0.5$  are shown in red.

		CO <sub>2</sub>	precession index	obliquity
		DJF_temperature	PC1	<b>-0.859</b>
PC2	0.381		-0.087	-0.354
PC3	0.038		<b>-0.924</b>	0.311
JJA_temperature	PC1	<b>-0.899</b>	0.178	-0.066
	PC2	-0.018	<b>-0.875</b>	0.362
	PC3	0.342	0.056	-0.239
DJF_precipitation	PC1	<b>-0.867</b>	0.003	-0.025
	PC2	-0.198	<b>-0.82</b>	0.044
	PC3	-0.278	0.465	0.164
JJA_precipitation	PC1	<b>-0.953</b>	0.065	0.008
	PC2	-0.07	<b>0.96</b>	-0.131
	PC3	0.219	0.191	-0.029

6

7

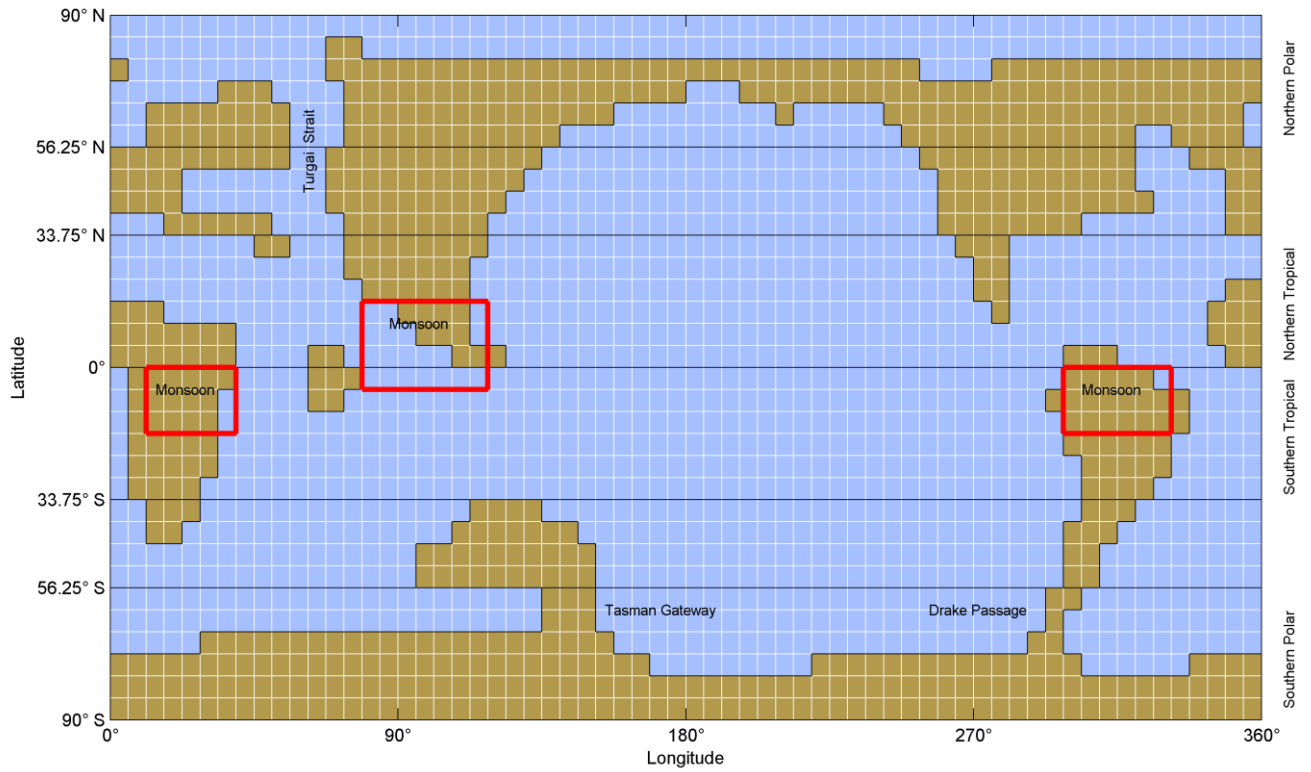
1 **Table 7** **Linear models derived from normalised forcing functions and monsoon indices**

<b>Terms</b>	<b>Asia</b>	<b>Africa</b>	<b>America</b>
<b>intercept</b>	-0.096	0.200	-0.273
<b>CO<sub>2</sub></b>	0.187	-0.089	-0.422
<b><math>\varepsilon</math></b>	0.189	0.027	0.065
<b><math>e</math></b>	0.049	-0.091	-0.070
<b><math>\sin(\omega)</math></b>	-0.577	0.510	0.309
<b><math>\cos(\omega)</math></b>	-0.114	-0.064	-0.105
<b>CO<sub>2</sub><sup>2</sup></b>	-	0.150	0.278
<b><math>e^2</math></b>	-	-0.115	-
<b><math>e \times \sin(\omega)</math></b>	-0.468	0.501	0.240
<b>CO<sub>2</sub> x <math>\sin(\omega)</math></b>	-0.214	0.215	-0.085
<b><math>\varepsilon \times \sin(\omega)</math></b>	-	-0.069	-0.071
<b><math>e \times \cos(\omega)</math></b>	-0.100	-	-
<b><math>\sin(\omega) \times \cos(\omega)</math></b>	0.118	-	-
<b><math>\varepsilon \times \cos(\omega)</math></b>	-	-0.121	-
<b>CO<sub>2</sub> x <math>\varepsilon</math></b>	0.121	-	-
<b>CO<sub>2</sub> x <math>\cos(\omega)</math></b>	-	0.098	-
<b>CO<sub>2</sub> x <math>e</math></b>	-	0.096	-

2

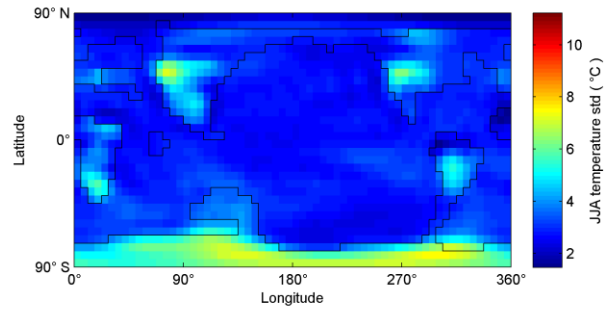
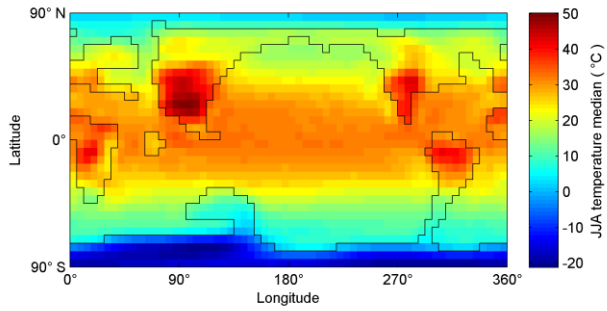
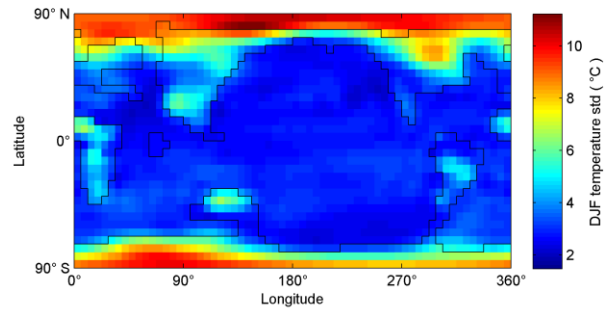
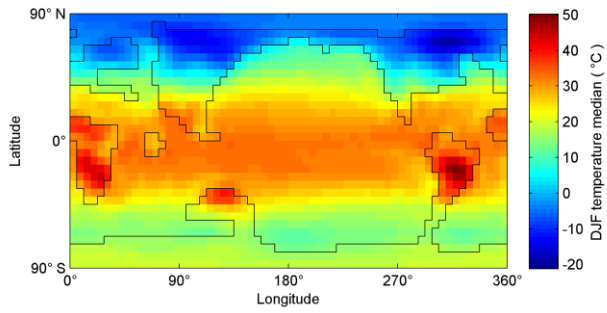
3

4



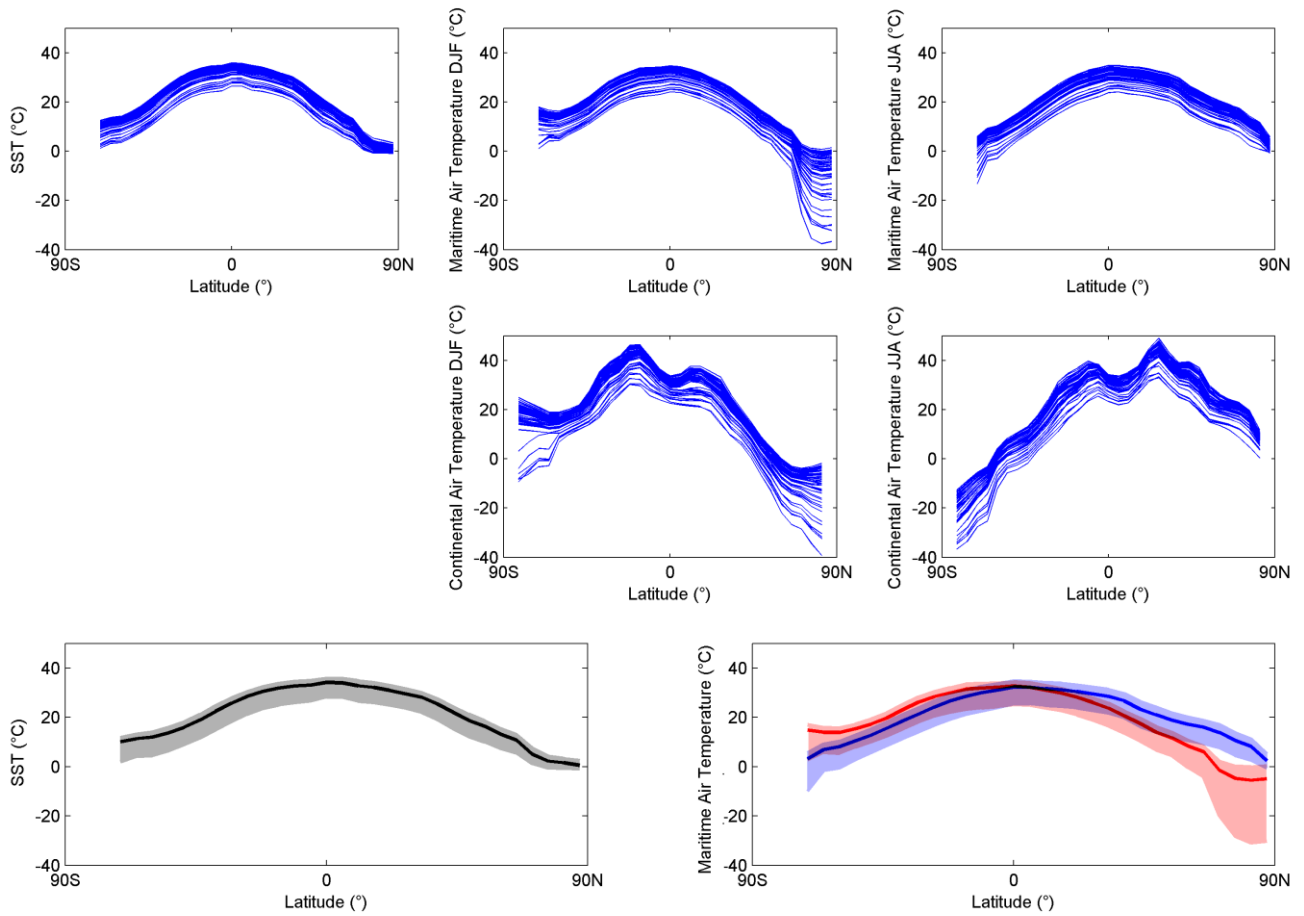
1  
2 **Figure 1: Eocene palaeogeography and geographic areas used to determine simple metric values**

3



1  
2  
3

**Figure 2: Ensemble temperature medians (left column) and standard deviations (right column) in DJF (top row) and JJA (bottom row).**



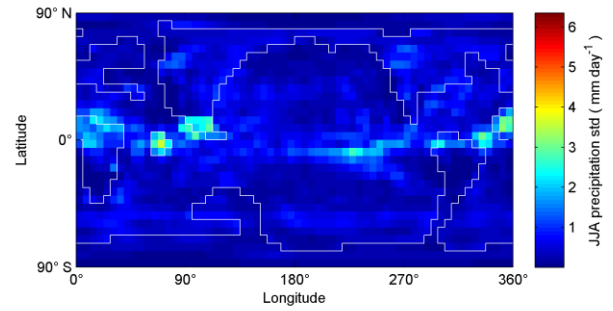
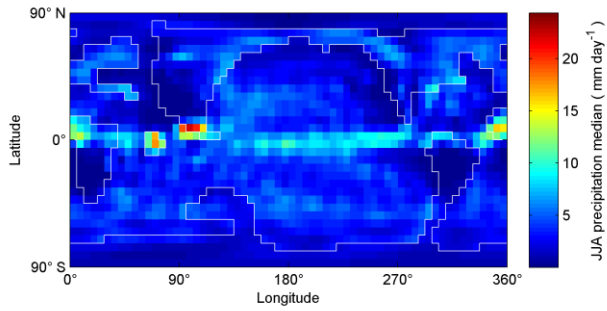
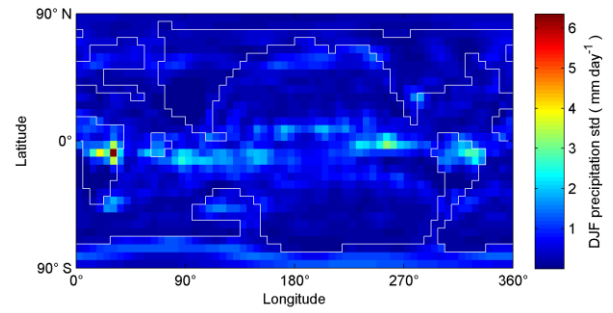
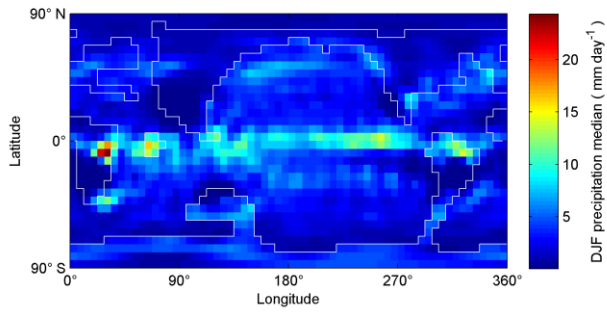
1

2 **Figure 3: Top: full ensemble distributions of mean latitude values of global annual mean sea surface temperature (SST), with**  
 3 **mean latitude maritime surface air temperature in DJF and JJA.**

4 **Middle: mean latitude continental surface air temperature in DJF and JJA.**

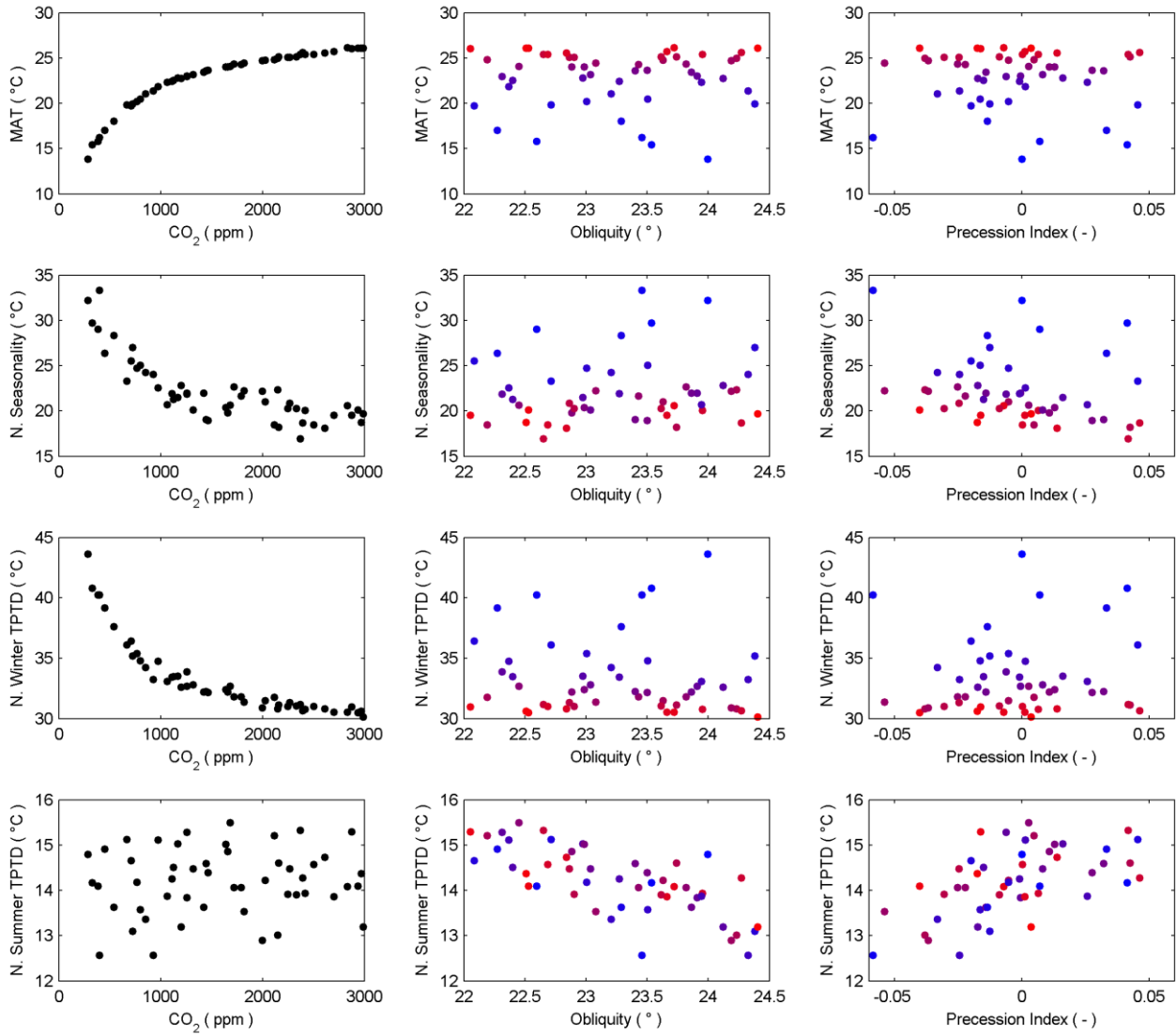
5 **Bottom: ensemble medians and 5% and 95% percentiles of global annual mean SST, and maritime surface air temperature in DJF**  
 6 **(red) and JJA (blue).**

7



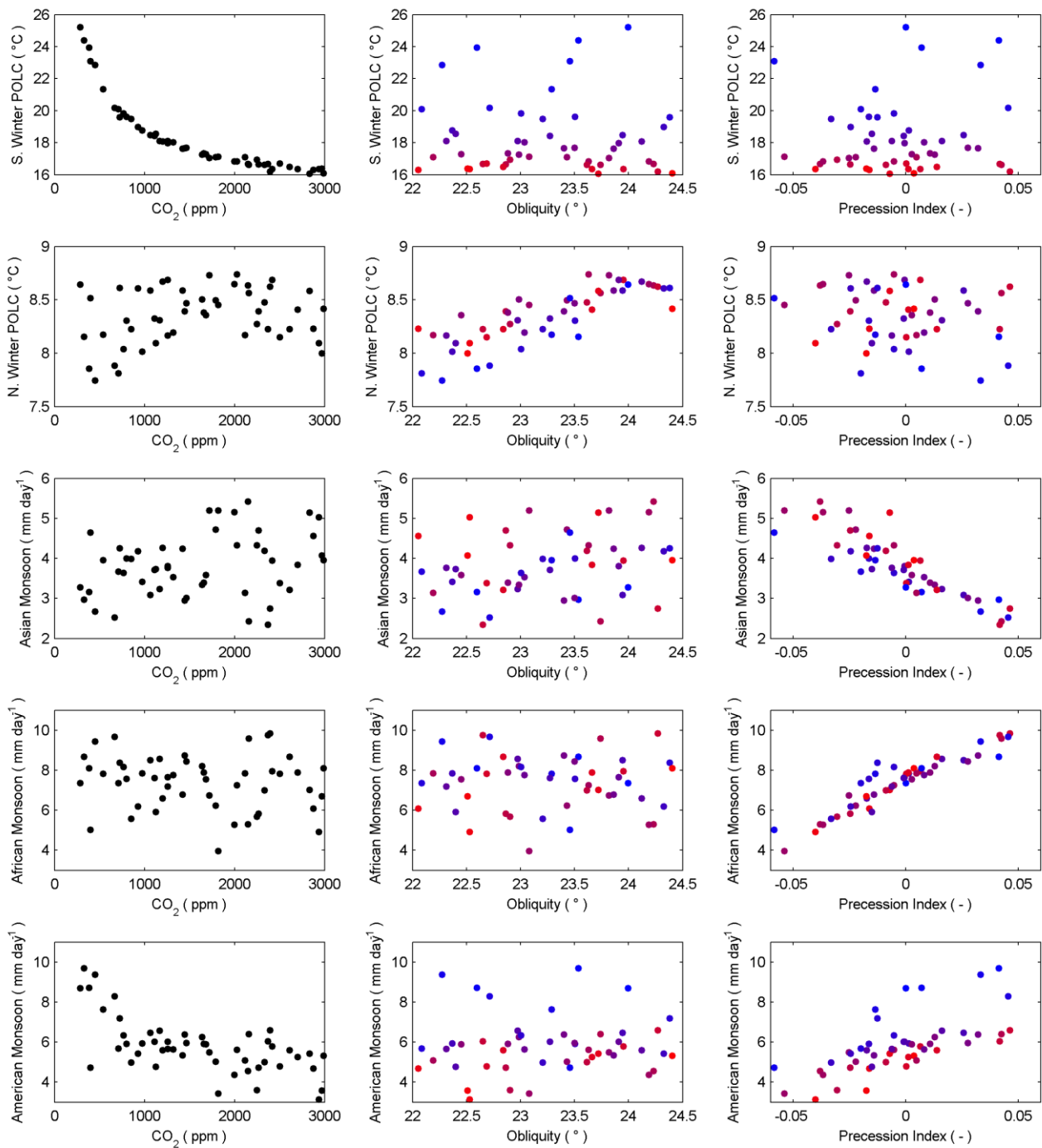
1  
2  
3

**Figure 4: Ensemble precipitation medians (left column) and standard deviations (right column) in DJF (top row) and JJA (bottom row).**



1  
 2 **Figure 5: Correlation between three forcing factors CO<sub>2</sub>, obliquity and precession index (in columns from left to right), and the**  
 3 **simple metrics MAT, northern seasonality, northern winter tropical-polar temperature difference and northern summer tropical-**  
 4 **polar temperature difference (in rows from top to bottom). CO<sub>2</sub> is plotted in colour in the obliquity and precession plots (blue =**  
 5 **low, red = high)**

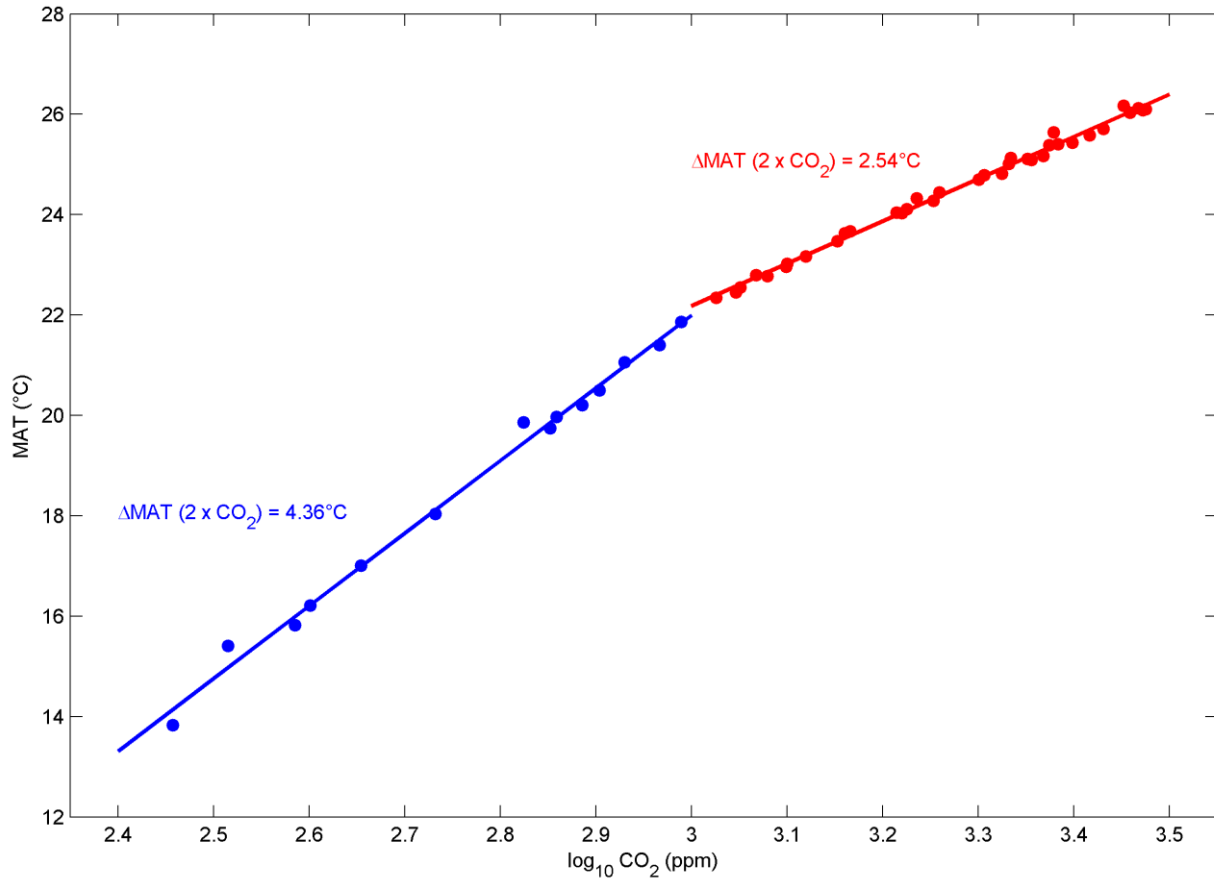
6



1 **Figure 6: Correlation between three forcing factors CO<sub>2</sub>, obliquity and precession index (in columns from left to right), and the**  
2 **simple metrics southern winter polar OLC, northern winter polar OLC, Asian monsoon index African monsoon index and**  
3 **American monsoon index (in rows from top to bottom). CO<sub>2</sub> is plotted in colour in the obliquity and precession plots (blue = low,**  
4 **red = high)**

5

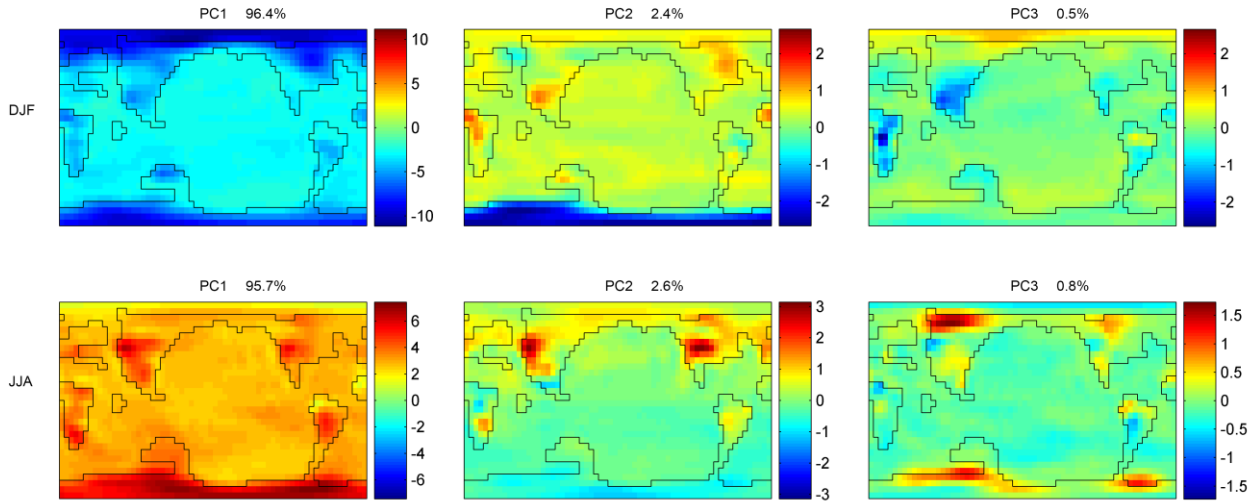
6



7

8 **Figure 7: Mean air temperature plotted against CO<sub>2</sub> on a logarithmic scale, with regression lines plotted for CO<sub>2</sub> < 1000 ppm**  
9 **(blue), and CO<sub>2</sub> > 1000 ppm (red), with climate sensitivities for a doubling of CO<sub>2</sub> from both of the regressions.**

1

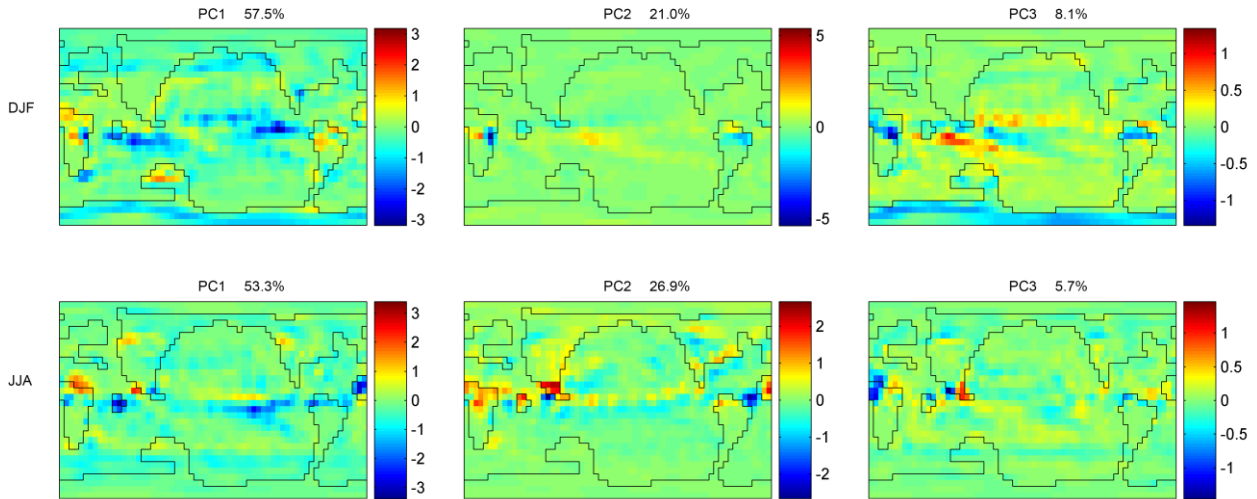


2

3 **Figure 8: The first three principal components of DJF\_temperature (top row) and JJA\_temperature (bottom row). Percentages of**  
4 **variance explained by each principal component are shown above each plot.**

5

6

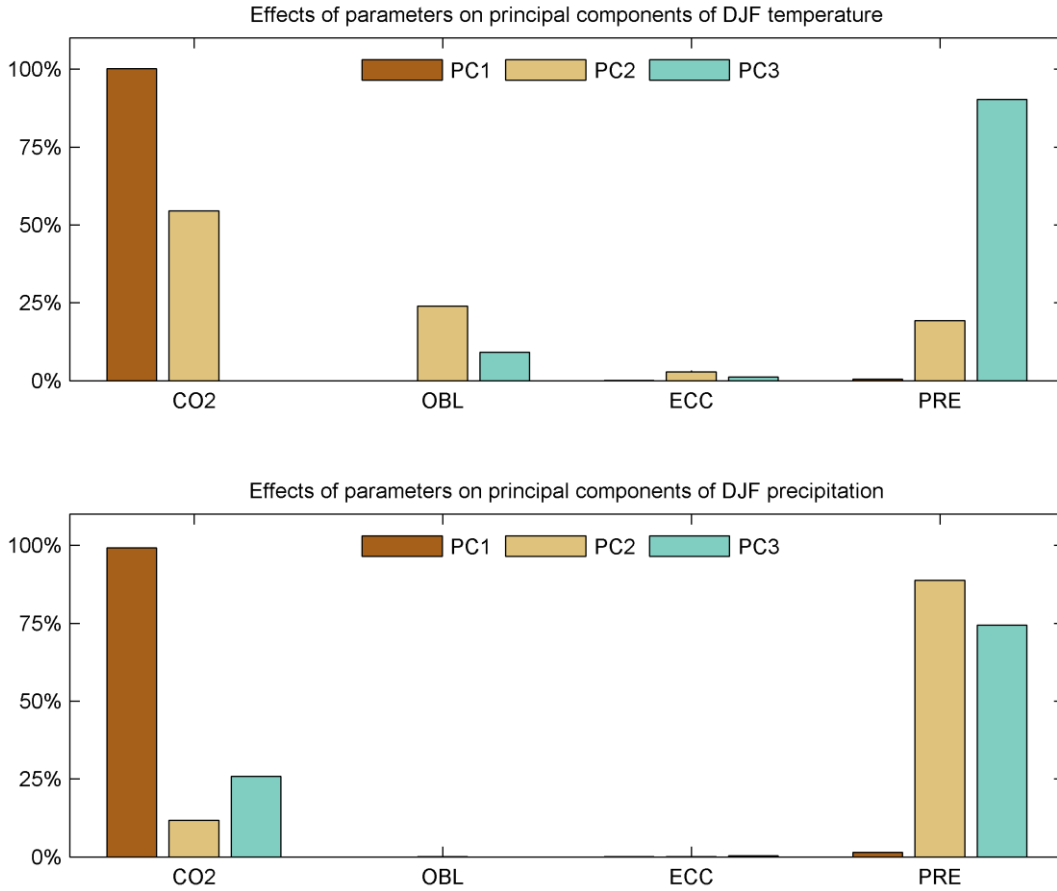


7

8 **Figure 9: The first three principal components of DJF\_precipitation (top row) and JJA\_precipitation (bottom row). Percentages of**  
9 **of variance explained by each principal component are shown above each plot.**

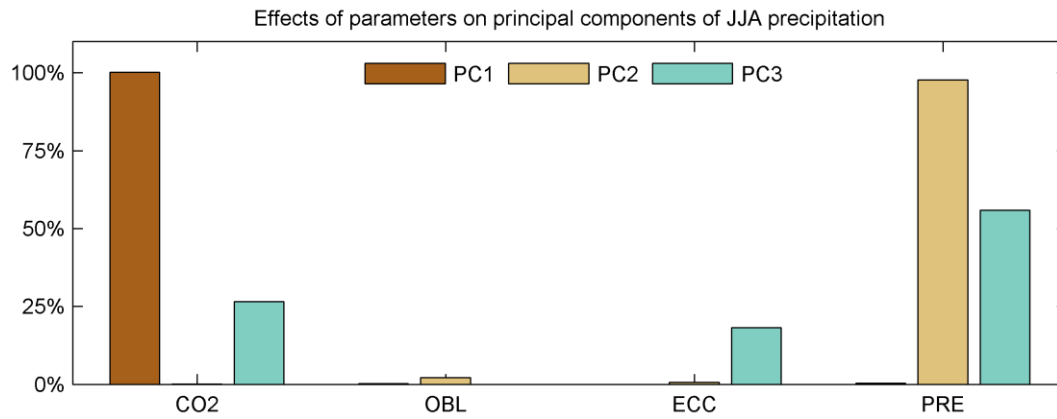
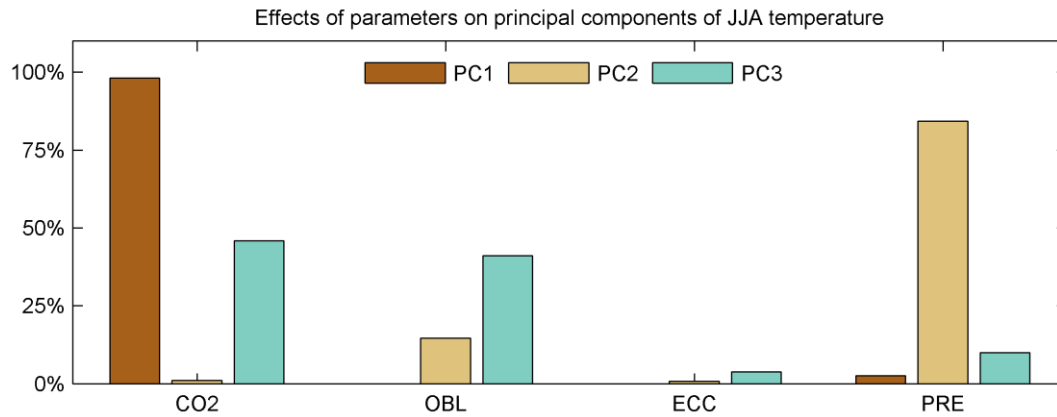
10

1  
2



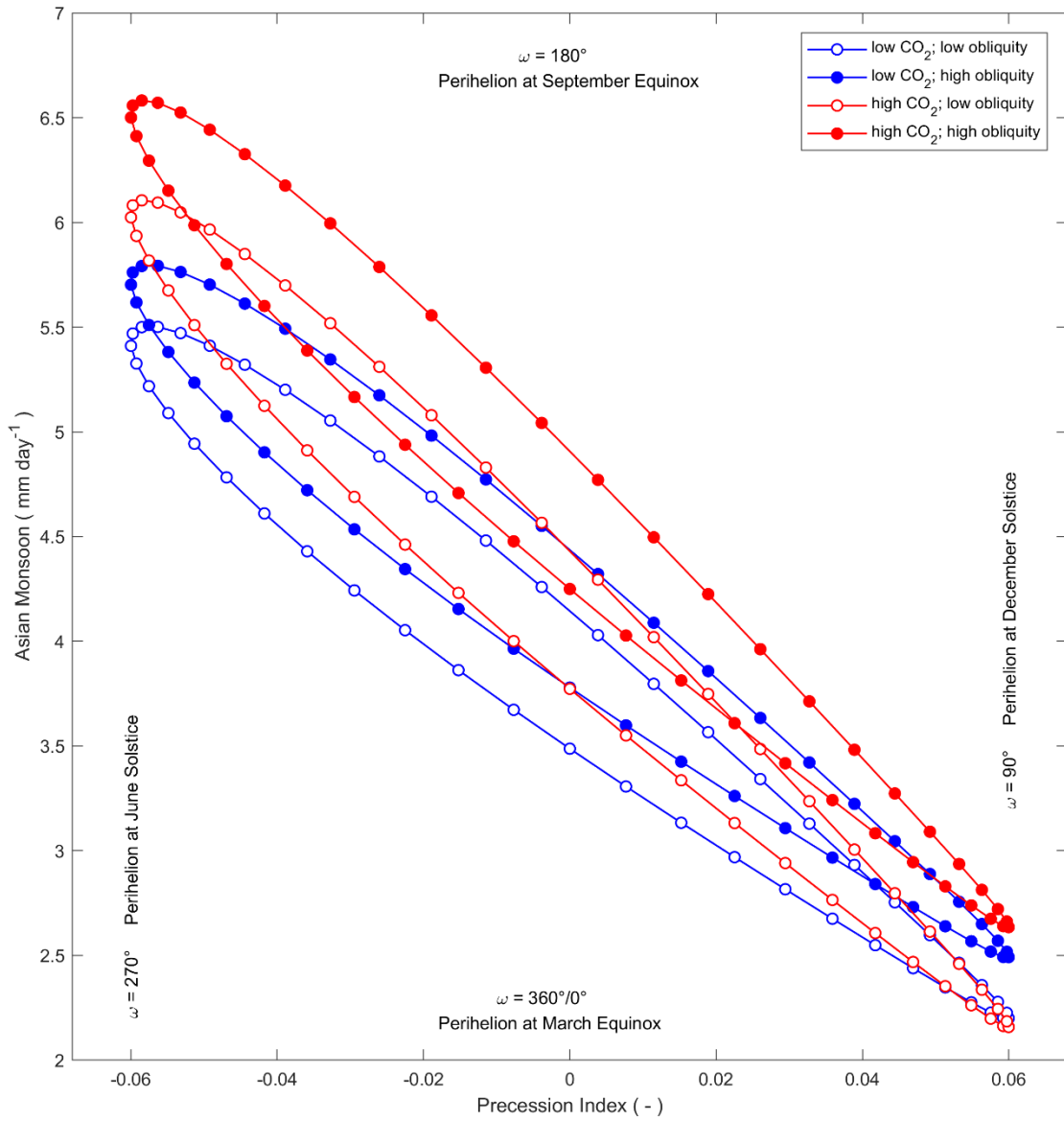
3  
4  
5  
6  
7  
8  
9

**Figure 10: Main effects of forcing parameters on the first three principal components of DJF\_temperature (top row) and DJF\_precipitation (bottom row).**

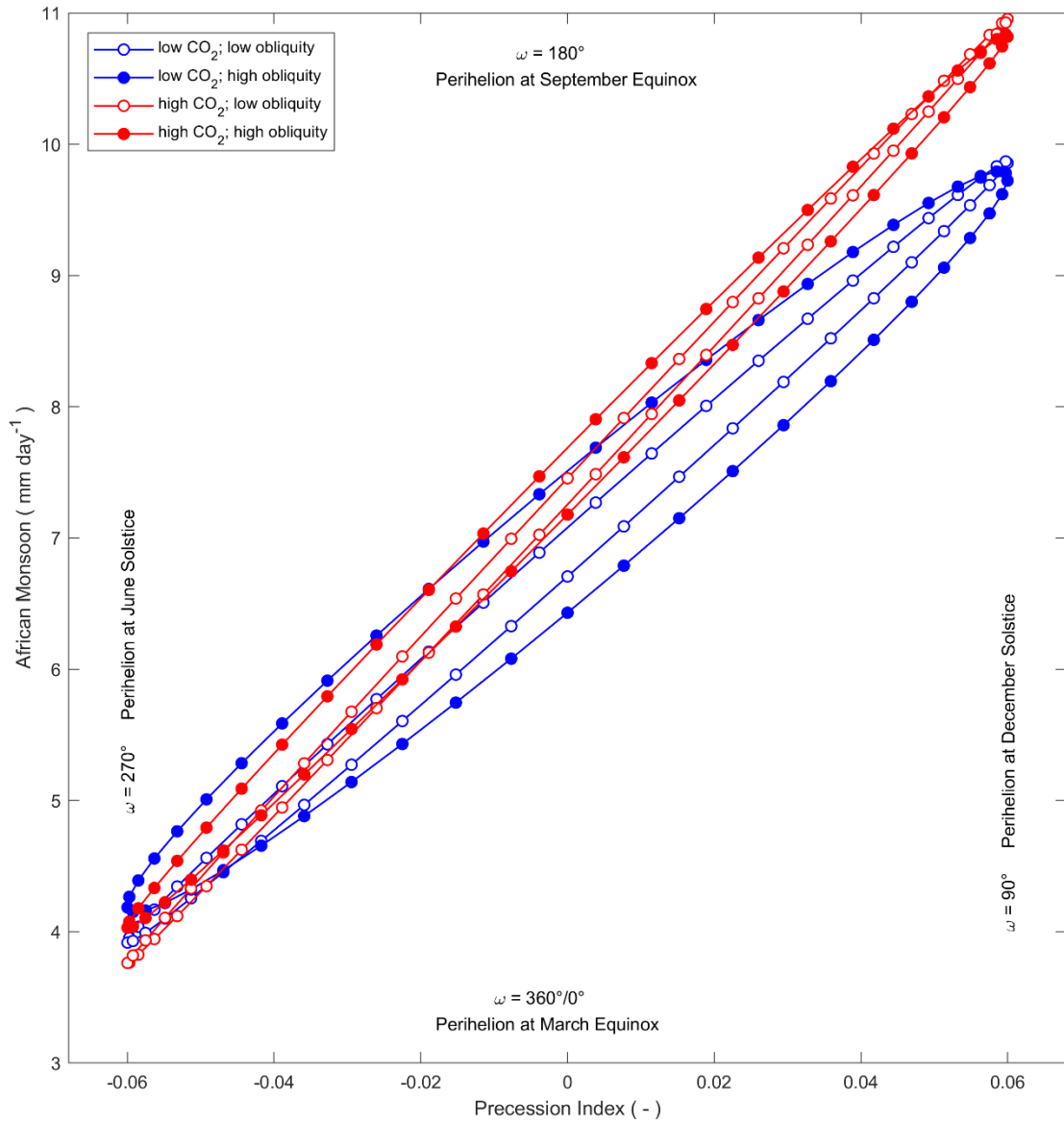


1

2 **Figure 11: Main effects of forcing parameters on the first three principal components of JJA\_temperature (top row) and**  
 3 **JJA\_precipitation (bottom row).**

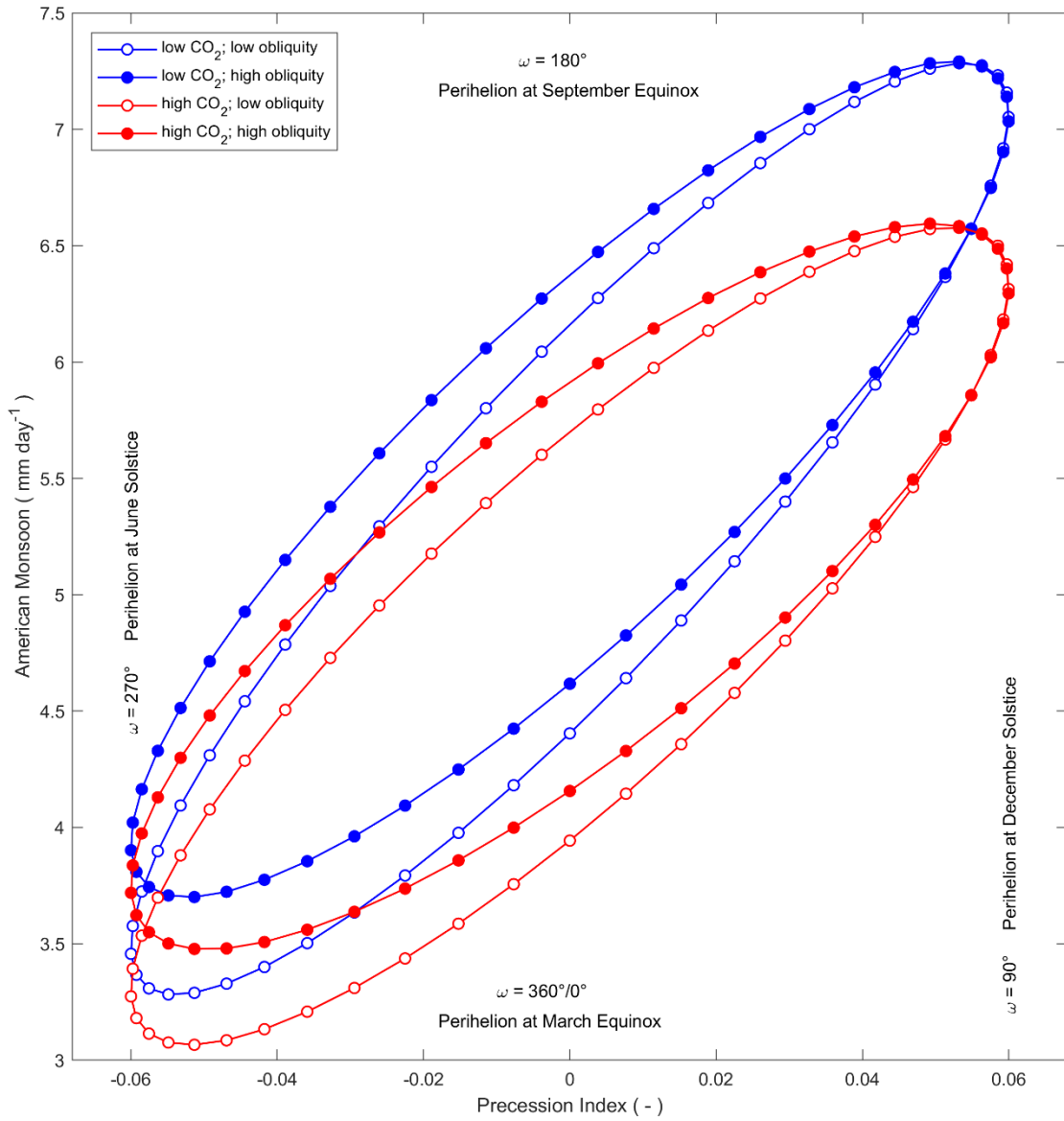


1  
 2 **Figure 12: Emulated values of the Asian monsoon index, for the full range of the precession index ( $\epsilon \sin \omega$ ), at low and high values**  
 3 **of  $\text{CO}_2$  and obliquity ( $\epsilon$ ).**



1

2 **Figure 13: Emulated values of the African monsoon index, for the full range of the precession index ( $\epsilon \sin \omega$ ), at low and high values**  
 3 **of CO<sub>2</sub> and obliquity ( $\epsilon$ ).**



1

2 **Figure 14: Emulated values of the American monsoon index, for the full range of the precession index ( $\epsilon \sin \omega$ ), at low and high**  
 3 **values of CO<sub>2</sub> and obliquity ( $\epsilon$ ).**